Network-based Molecular Constraints on *in vivo* Synaptic Density Alterations in Schizophrenia

Sidhant Chopra[1-3], Patrick D. Worhunsky[4], Mika Naganawa[5], Xi-Han Zhang[1], Ashlea Segal[6] Edwina Orchard[1,7], Vanessa Cropley[2,3], Stephen Wood[2,3,8], Gustavo A. Angarita[4], Kelly Cosgrove[4], David Matuskey[4,5], Nabeel B. Nabulsi[5], Yiyun Huang[5], Richard E. Carson[5], Irina Esterlis[1,4,5], Patrick D. Skosnik[4], Deepak C. D'Souza[4], Avram J. Holmes[9]*, Rajiv Radhakrishnan[4,5]*

1. Department of Psychology, Yale University, New Haven, CT, USA
2. Orygen, Parkville, Melbourne, VIC, Australia
3. Centre for Youth Mental Health, The University of Melbourne, Melbourne, VIC, Australia
4. Department of Psychiatry, Yale University, New Haven, CT, USA
5. Department of Radiology and Biomedical Imaging, Yale University, New Haven, CT, USA
6. Department of Neuroscience, Yale University, New Haven, CT, USA
7. Ann S. Bowers Women's Brain Health Initiative, University of California Santa Barbara, CA, USA
8. School of Psychology, University of Birmingham, UK
9. Department of Psychiatry, Brain Health Institute, Rutgers University, Piscataway, NJ, USA

*These authors have contributed equally to this work.

Corresponding Author: Sidhant Chopra (sidhantchopra4@gmail.com; sidhant.chopra@orygen.org)

Abstract

Converging neuroimaging, genetic, and post-mortem evidence show a fundamental role of synaptic deficits in schizophrenia pathogenesis. However, the underlying molecular and cellular mechanisms that drive the onset and progression of synaptic pathology remain to be established. Here, we used synaptic density positron emission tomography (PET) imaging using the [^{11}C]UCB-J radiotracer to reveal a prominent widespread pattern ($p_{FWE} < 0.05$) of lower synaptic density in individuals with schizophrenia (n=29), compared to a large sample of healthy controls (n=93). We found that the spatial pattern of lower synaptic density in schizophrenia is spatially aligned ($r_{cca} = 0.67$; $p < 0.001$) with higher normative distributions of $GABA_{A/BZ}$, $5HT_{1B}$, $5HT_{2A}$, and $5HT_6$, and lower levels of CB_1 and $5HT_{1A}$. Competing neighborhood deformation network models revealed that regional synaptic pathology strongly correlated with estimates predicted using a model constrained by both interregional structural connectivity and molecular similarity ($.42 < r < .61$; $p_{FWE} < 0.05$). These data suggest that synaptic pathology in schizophrenia is jointly constrained by both global axonal connectivity and local molecular vulnerability. Simulation-based network diffusion models were used to identify regions that may represent the initial sources of pathology, nominating left prefrontal areas ($p_{FWE} < 0.05$) as potential foci from which synaptic pathology initiates and propagates to molecularly similar areas. Overall, our findings provide *in vivo* evidence for widespread deficit in synaptic density in schizophrenia that is jointly constrained by axonal connectivity and molecular similarity between regions, and that synaptic deficits spread from initial source regions to axonally connected and molecularly similar territories.

Decades of post-mortem research has demonstrated lower dendritic spine density and molecular markers of synaptic integrity[1, 2] in individuals with schizophrenia, suggesting that loss of synapses is a fundamental pathophysiological process in schizophrenia. Recent large-scale genetic studies in patients have robustly implicated genes related to synaptic elimination, formation, and plasticity, indicating that the synapse is a principal site of pathology in schizophrenia[3, 4]. Until recently, synaptic quantity in the human brain could only be measured post-mortem. The advent of positron emission tomography (PET) radioligands that bind to vesicular proteins now make it possible to examine synaptic terminal density *in vivo*[5]. Preliminary studies using these PET ligands[6] in individuals with early[7, 8] and chronic[9, 10] schizophrenia align with post-mortem and genetic findings, demonstrating regionally lower synaptic density in cingulate, temporal and frontal regions, especially in chronic illness[9, 10].

Synaptic pathology, such as loss, is a process that occurs as an interaction between the synapse and its genetic, neurochemical, and cellular environment. The specific genetic, neurochemical, and cellular mechanisms underlying synaptic pathology in schizophrenia remain unknown. Several biological mechanisms have been proposed, including altered neurodevelopment[11, 12], immune-mediated glial hyperactivity[3, 13], excitotoxic neurochemical abnormalities[14, 15] and dysregulated protein homeostasis[16, 17]. Research into other neurological conditions has demonstrated differential pathological vulnerability of brain regions based on characteristics such as large-scale functional systems[18], cell-types[19] and receptor[20] composition. The molecular composition of a region may therefore confer differential risk of pathology. However, regional molecular vulnerabilities in isolation may not alone account for the distributed patterns of synaptic pathology observed in schizophrenia, as regions are embedded within interconnected axonal and functional networks that shape pathological spread, facilitate compensatory responses, and enable emergent vulnerabilities through altered network topology[21, 22].

Work in neurological disorders has demonstrated a pivotal role of macroscale axonal networks in shaping brain pathology. The brain is comprised of an intricate network of axonal connections that link functionally interacting neuronal populations. These connections are essential for brain function, as well as the transport of biological molecules throughout the brain. In neuropsychiatric diseases, illness processes, including disrupted synaptic transmission or molecular agents, can propagate along these axonal connections[23]. The progression of illness-related gray matter loss, constrained by axonal connections, has now been consistently demonstrated in both early and later stages of psychotic illnesses[22, 24], suggesting pathophysiology may propagate trans-neuronally[22]. However, axonally connected regions share genetic, neurochemical, cellular, and functional properties[25], raising the question of whether observed patterns of pathology are driven by connectivity itself, by these shared properties, or by their interaction[26-28].

Here, we fill this critical gap by demonstrating a brain-wide pattern of lower synaptic terminal density in the living human brain of people with schizophrenia, using [^{11}C]UCB-J radiotracer PET imaging from a large single-site sample of 122 individuals, including 29 with schizophrenia. We find that synaptic loss is preferentially located within the functional frontoparietal network and relatively spared in limbic networks. We go on to use network models to demonstrate that a given region's synaptic profile is tightly coupled with corresponding alterations in axonally connected and molecularly similar neighboring regions. Finally, using network diffusion models, our findings suggest that synaptic deficit in psychotic

illness may follow a predictable pattern of propagation, spreading from initial source regions in the left inferior frontal cortex to axonally connected and molecularly similar brain areas.

Results

Synaptic density is lower across the brain in schizophrenia

Numerous studies have now used *in vivo* synaptic density PET imaging to examine differences between individuals with early psychosis or schizophrenia and healthy control populations[7-10]. These data are in line with prior genetic[3, 4], post-mortem[1, 2] and induced pluripotent stem cell work[29-32] demonstrating lower markers of synaptic integrity in patients, albeit with more circumscribed alterations during the earlier stages of illness[8]. To date, synaptic density PET imaging studies in psychosis largely use a region-of-interest approach where limited areas are selected a priori and differences in average levels of tracer binding metrics are compared. Here, using the [^{11}C]UCB-J radiotracer and the largest *in vivo* synaptic density imaging sample to date, we take an unbiased whole-brain voxel-level approach to examine differences between individuals with schizophrenia and healthy controls (see Table 1 for details). After implementing motion correction and kinetic modelling, we derived partial volume corrected and spatially standardized parametric images that indexed non-displaceable binding potential (BP_{ND}) for each individual (see Methods for details). Here, we used BP_{ND} as it is highly specific to synaptic vesicle density[33-35], and sensitive to detecting synaptic abnormalities in schziophrenia[7, 9]. Voxel-level brain-wide group differences in synaptic density were examined after adjusting for age and sex. We found prominent and widespread lower synaptic density in individuals with schizophrenia (Fig. 1A), compared to controls, with frontal, temporal, cingulate, thalamic, striatal and hippocampal areas surviving stringent voxel-level family-wise error (FWE) correction ($p_{FWE} < 0.05$, Fig. 1A), and with the left hemisphere generally showing higher levels of synaptic deficits then the right hemisphere. We repeated our analyses after adjusting for antipsychotic medication exposure (SFig. 1A), after excluding individuals with a history of substance abuse (SFig. 1B), and after removing partial volume correction (SFig. 1C), finding a highly similar and significantly correlated pattern of lower synaptic density. Mean voxel-level BP_{ND} maps for patients and controls are provided in SFig. 2)

Table 1. Sample Demographics

	Schizophrenia (N=29)	Control (N=93)	p-value
Age, mean years (SD)	43.21 (14.66)	45.40 (16.83)	0.501
Females, N (%)	4 (13.8%)	37 (39.8%)	0.018
Mass dose, mean in ug/kg (SD)	0.02 (0.02)	0.02 (0.02)	0.647
Activity at time of injection, mean MBq (SD)	235.53 (201.00)	194.61 (125.28)	0.332
Antipsychotic exposure, mean CPZ eqs. (SD)	2693.34 (2738.91)	-	-
PANSS Total, mean (SD)	68.39 (13.51)	-	-
PANSS Positive, mean (SD)	17.46 (5.26)	-	-

PANSS Negative, mean (SD)	16.64 (5.06)	-	-
PANSS General, mean (SD)	33.93 (6.88)	-	-

CPZ eqs. = lifetime exposure to antipsychotics as chlorpromazine (CPZ) equivalents (eqs.). Listed p-values correspond to two-sample t-tests, except for gender-differences, where they correspond to a X^2 proportion test. PNASS= Positive and Negative Syndrome Scale.

Computed tomography (CT) and magnetic resonance imaging (MRI) studies have demonstrated lower gray matter volume across different stages of psychosis[36-43]. The neural substrate underlying reported MRI signal alterations remains unknown. Despite limited empirical evidence, it is theorized that these signal changes result, in part, from a loss of synapses[44-46]. To test this hypothesis, we examined whether the detected synaptic alterations were spatially consistent with gray matter volume alterations within the current sample as well as in four independent patient cohorts spanning different stages of psychotic illness: medication-naive first-episode psychosis[41] ($N_{case/control}$=59/27), early psychosis[47] ($N_{case/control}$=121/57), and established schizophrenia[48, 49] ($N_{case/control}$=66/72; $N_{case/control}$=70/62). We first parcellated the synaptic alteration map (Fig. 1A) and gray matter volume alteration maps from the current and four independent patient cohorts into 332 discrete cortical[50] and subcortical[51] regions. Product-moment correlations were significance-tested using non-parametric spatial autocorrelation preserving null models (see Methods for details)[52, 53]. Overall, the spatial patterns of synaptic and volumetric alteration were not correlated within the current sample ($r = 0.01$; $p = .672$), nor across four independent samples ($-0.11 < r < -0.02$; $ps > 0.078$; Fig. 1C). This was not because the current sample was neuroanatomically distinctive, since there were significant correlations between the volume alteration maps of the current sample and those from other datasets ($.28 < r < .39$; $p_{FWE} < 0.05$), except for the first episode psychosis dataset ($r = .15$; $p = .121$). Results remained consistent when partial volume correction was not implemented for the synaptic density maps (SFig. 3A) and when deformation-based, rather than voxel-based, morphometry was used to measure gray matter volume differences between groups (SFig. 3B).

Consistent with post-mortem, genetic and *in vitro* findings, our results demonstrate prominent and wide-spread *in vivo* synaptic alterations in schizophrenia, which are spatially independent of commonly reported MRI-derived gray matter volume alterations across different stages of illness.

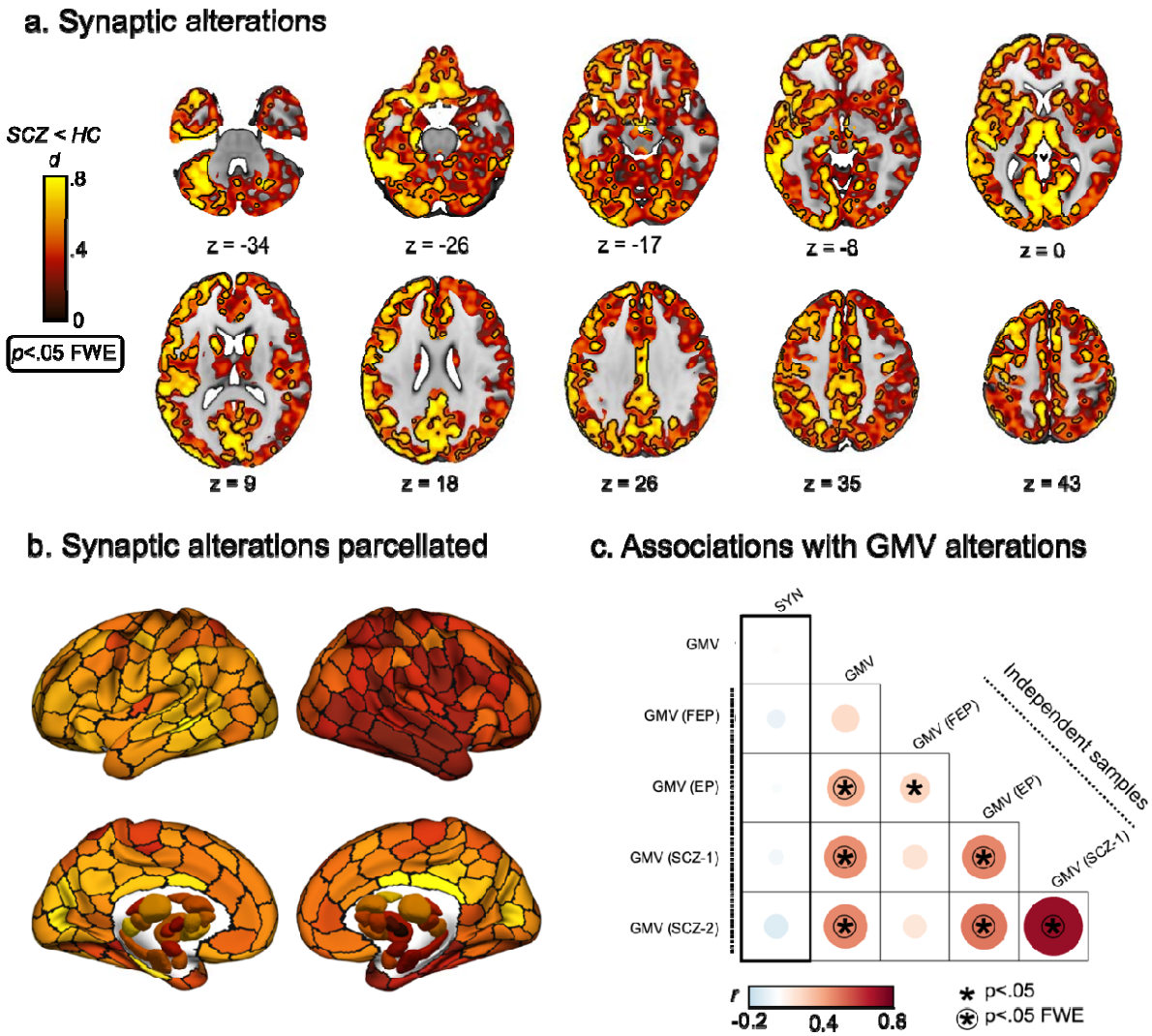

Fig. 1. Wide-spread lower synaptic density in schizophrenia. **a)** Voxel-level effect-size map of difference in binding potential (non-displaceable) between individuals with schizophrenia (SCZ) and healthy controls (HC), adjusting for age and sex. Test statistics (t-values) were converted to standardized effect-sizes (Cohens *d*) for visualization. Black outline indicated voxel-level family wise error corrected (FWE) significance at p<0.05. **b)** Effect-size map parcellated using the cortical Schaefer 300 regions and subcortical Tian 32 region atlases, with the mean value of voxels assigned to each region. **c)** Black outline highlights spatial correlation (Pearsons r) between parcellated synaptic density alterations (SYN) and gray matter volume (GMV) within the current sample (top left box), as well as four independent samples including antipsychotic-naive first-episode psychosis (FEP), early psychosis (EP) and two established schizophrenia (SCZ) cohorts. All other boxes represent correlations between GMV maps between the current and independent samples. Asterisks (*) indicate statistical significance ( ) completed to spatial autocorrelation preserving null models, with a circle indicating survival against FWE correction.

Network and molecular enrichment of synaptic pathology

Brain alterations in psychiatric and neurological disorders, such as gray matter loss, preferentially affect specific systems such as macroscale functional networks and distinct cytoarchitectonic regions[19, 26, 54]. This spatial organization of pathology suggests that the functional and cellular properties of distributed brain regions may confer differential vulnerability to disease processes. To examine preferential accumulation of synaptic pathology across functional and cytoarchitectonic systems we used two brain system classifications: i) intrinsic cortical functional networks based on the Yeo 17-network[50, 55] classification and ii) cytoarchitectonic[56] types of laminar differentiation based on the canonical von Economo and Koskinas atlas[57]. We examined system-level pathology by averaging the effect size of synaptic deficit (Fig. 1B) across regions within each intrinsic network or cytoarchitectonic subdivision. We tested the significance of these empirical values against null distributions of means calculated from a set of spatial autocorrelation-preserving null models[52, 53] (see Methods). After FWE-correction, we find that aspects of the functional frontoparietal/cognitive control networks, particularly dorsal precuneus and posterior cingulate areas (FPN C subdivision), are especially vulnerable to synaptic pathology ($Z = 2.28$; $p_{FWE} = .048$; Fig. 2A), whereas limbic networks comprising inferior and polar temporal cortices are relatively resilient ($Z = -2.29$; $p_{FWE} = .010$; Fig. 2A). No significant enrichment was observed for any cytoarchitectonic types of laminar differentiation (SFig. 4).

Next, we examined whether the cellular and neurochemical composition of a region was associated with vulnerability to synaptic pathology. First, we characterized the normative brain-wide regional concentrations of i) 24 receptors and transporters[58] and ii) 24 transcriptomically defined cell types[59, 60]. The receptor and transporter maps were derived from group-level PET data from healthy subjects and collated using the *neuromaps* toolbox[58]. Each neurochemical map was parcellated using the same whole-brain atlas used in the prior analyses, with the mean tracer binding metric assigned to the corresponding region. The cell-type concentrations at each cortical region were deconvolved from whole brain bulk tissue transcriptions provided by the Allens Human Brain Atlas[61] with 24 different cell types imputed using single-nucleus RNA-sequencing[59] (see Methods and elsewhere[60] for details). Each cell-type map was parcellated using the same cortical atlas used in the prior analysis. To investigate the impact of neurochemical and cellular composition on synaptic pathology, we computed two independent multivariate canonical correlation analyses (CCA)[62], where we characterized the spatial coupling between either the regional receptor/transporter concentrations or cell-type densities and regional synaptic pathology. The resulting canonical correlation coefficient was compared to null values derived using spatial-autocorrelation-preserving null models (see Methods). We found that the normative receptor/transporter ($r_{cca} = .69$; $p < .001$; Fig. 2C), but not cell-type ($r_{cca} = .34$; $p = .56$; SFig. 5), concentrations were spatially coupled with the magnitude of synaptic pathology. When examining the canonical loadings of each receptor/transporter, we found that regions with typically higher concentrations of $5HT_{2A}$, $5HT_{1B}$, and $GABA_{A/BZ}$, and regions with typically lower concentrations of CB_1 and $5HT_{1B}$ receptors, were reliably ($p_{FWE} < 0.05$) associated with worse synaptic pathology in individuals with schizophrenia.

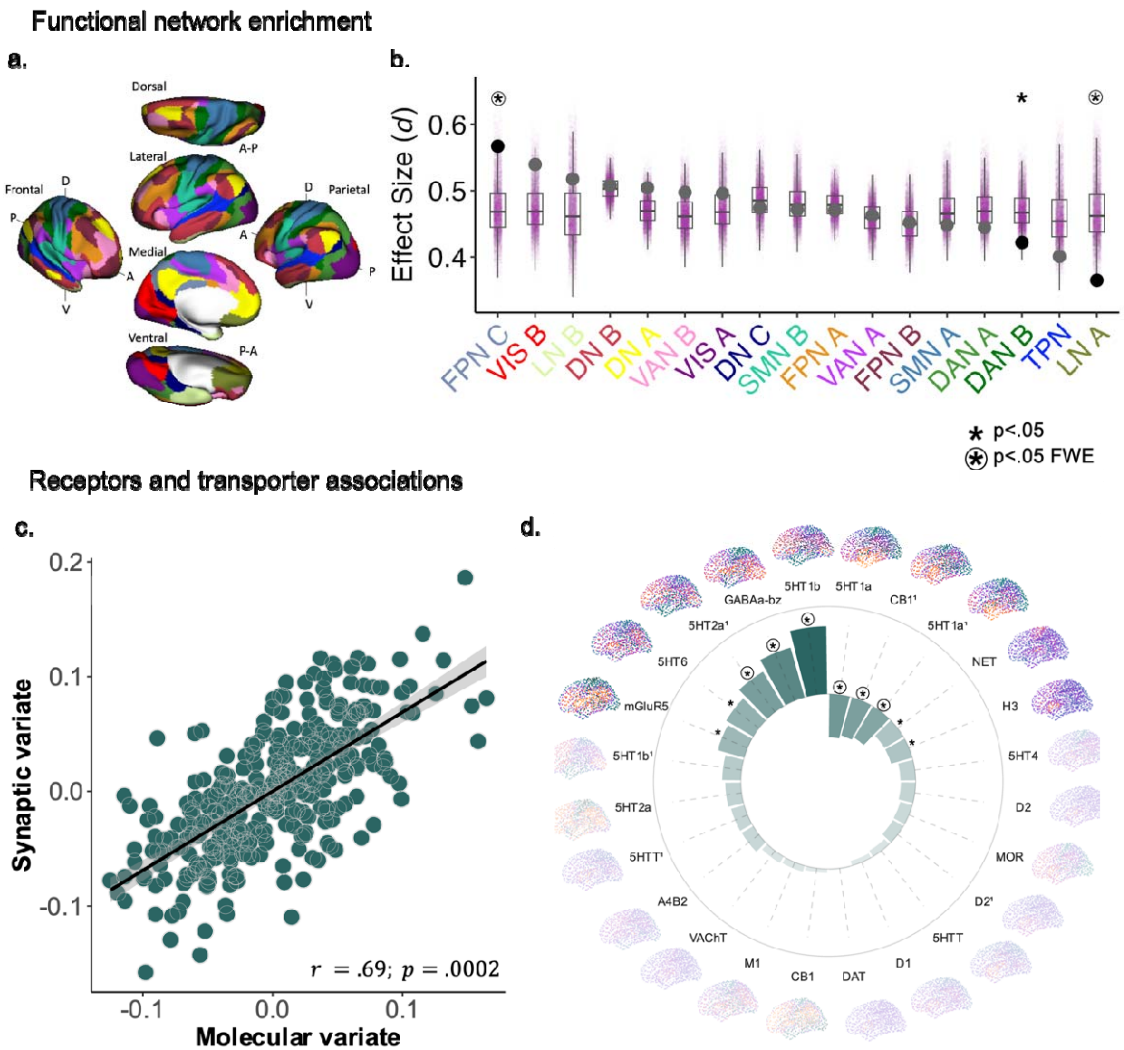

Fig. 2. Network and neurochemical predictors of synaptic pathology in schizophrenia. a) Whole-brain 17-network functional network partition[50, 55] across the cortex. TPN: temporal parietal network, DN: default network, FPN: frontoparietal network (sometimes referred to as cognitive control network), LN: limbic network, VAN: salience/ventral attention network, DAN: dorsal attention network, SMN: somatomotor network, VIS: visual network. **b)** Boxplots showing preferential accumulation of synaptic deficits within each of the 17 networks. Black dots represent observed mean effect-size of lower synaptic density in individuals with schizophrenia, with purple dots representing null mean effect sizes generated using spatial-autocorrelation preserving models. Asterisks (*) indicates statistical significance ( ), with a circle indicating survival against family-wise error (FWE) correction. **c)** Canonical correlation between regional synaptic deficits and normative receptor/transporter density. The synaptic variate (y-axis) in this case is normalized regional synaptic deficit effect size, whereas the molecular/neurochemical variate is a normalized weighted combination of regional receptor/transporter densities. The non-parametric -value was computed using spatial-autocorrelation preserving models. **d)** Loadings of each receptor/transporter map onto the significant neurochemical variate. Super-script numbers indicate different radiotracers for the same receptor/transporter. Asterisks (*) indicates statistical significance using bootstrapping (p<0.05), with a circle indicating survival of FWE-correction. Canonical correlation between regional synaptic deficits and normative cell-type density are provided in SFig. 5.

Axonal connectivity and molecular similarity jointly constrain synaptic alterations in schizophrenia

In schizophrenia, anatomical alterations are often correlated across spatially distributed regions[63-66], corresponding with normative connectome organization[67, 68], and are consistent with network-based spreading constrained by axonal connectivity[22, 24]. While these findings suggest that axonal connectivity is a powerful network-level constraint on brain pathology in schizophrenia, an alternative explanation for these findings is that regions sharing a strong anatomical connection also share similar functional, neurochemical, genetic, or cellular profiles, resulting in a shared vulnerability to illness-related alterations that target one or more of these features.

To disentangle whether synaptic alterations in schizophrenia are constrained by connectivity, regional vulnerabilities, or a combination thereof, we tested multiple competing neighborhood deformation models. In the neighborhood deformation model[24], a region's pathology is predicted by the mean pathology of its structurally connected neighboring regions (Fig 3A), optionally weighted by the strength of connectivity to the index region (see Methods for details). We tested three broad classes of neighborhood deformation models that respectively assess the contribution of 1) axonal connectivity, 2) regional vulnerability, or 3) a combination of these constraints, on synaptic pathology. The two connectivity models follow a similar form to previously used neighborhood deformation models[22, 24], where each region's synaptic pathology is predicted by the average synaptic pathology of axonally connected neighbors, either unweighted or weighted by connectivity strength. Axonal connectivity was estimated using a group-consensus connectivity matrix derived from tractography applied to the high-resolution diffusion-weighted imaging data from the Human Connectome Project (Fig. 3B, see Methods). The joint models, which test the combined effect of connectivity and regional vulnerability, weighted the neighboring regions' synaptic pathology by the similarity of one of five different features: function (i.e., hemodynamic coupling), receptor/transporter expression, cell type abundance, gene expression, and schizophrenia-related risk gene expression (Fig. 3B). Each of these feature similarity matrices were derived from independent datasets and used separately to weight each neighborhood deformation model (see Methods for details regarding derivation of feature similarity matrices). Therefore, if an axonally connected neighboring region shared a similar feature, such as commonalties in cell types, the contribution of the synaptic pathology of that neighboring region was accordingly upweighted in the prediction. The regional vulnerability models followed the same form as the joint models but removed the constraint of connectivity and predicted a region's synaptic pathology by all other regions, not just axonally connected neighbors, weighted by one of the five feature similarity matrices. Overall, we tested 12 different competing models within each hemisphere. Model performance was evaluated as the product-moment correlation between observed and model-predicted spatial pattern of synaptic pathology, and observed coefficients were compared to null values derived using spatial-autocorrelation preserving null models (Fig. 3A).

We found that the best-performing model considers the joint effect of axonal connectivity and receptor/transporter similarity in both the right ($r = .62$) and left ($r = .42$) hemispheres (Fig. 3C-D). The model reached FWE significance in both hemispheres ($p_{FWE} < 0.05$). Models considering the joint effect of axonal connectivity and gene expression similarity also performed well within the left hemisphere, albeit not reaching significance. Overall, these findings demonstrate that synaptic pathology of a region is closely associated with pathology in axonally connected and molecularly similar brain

regions, suggesting that connectivity and regional molecular vulnerability jointly shape synaptic alterations in schizophrenia.

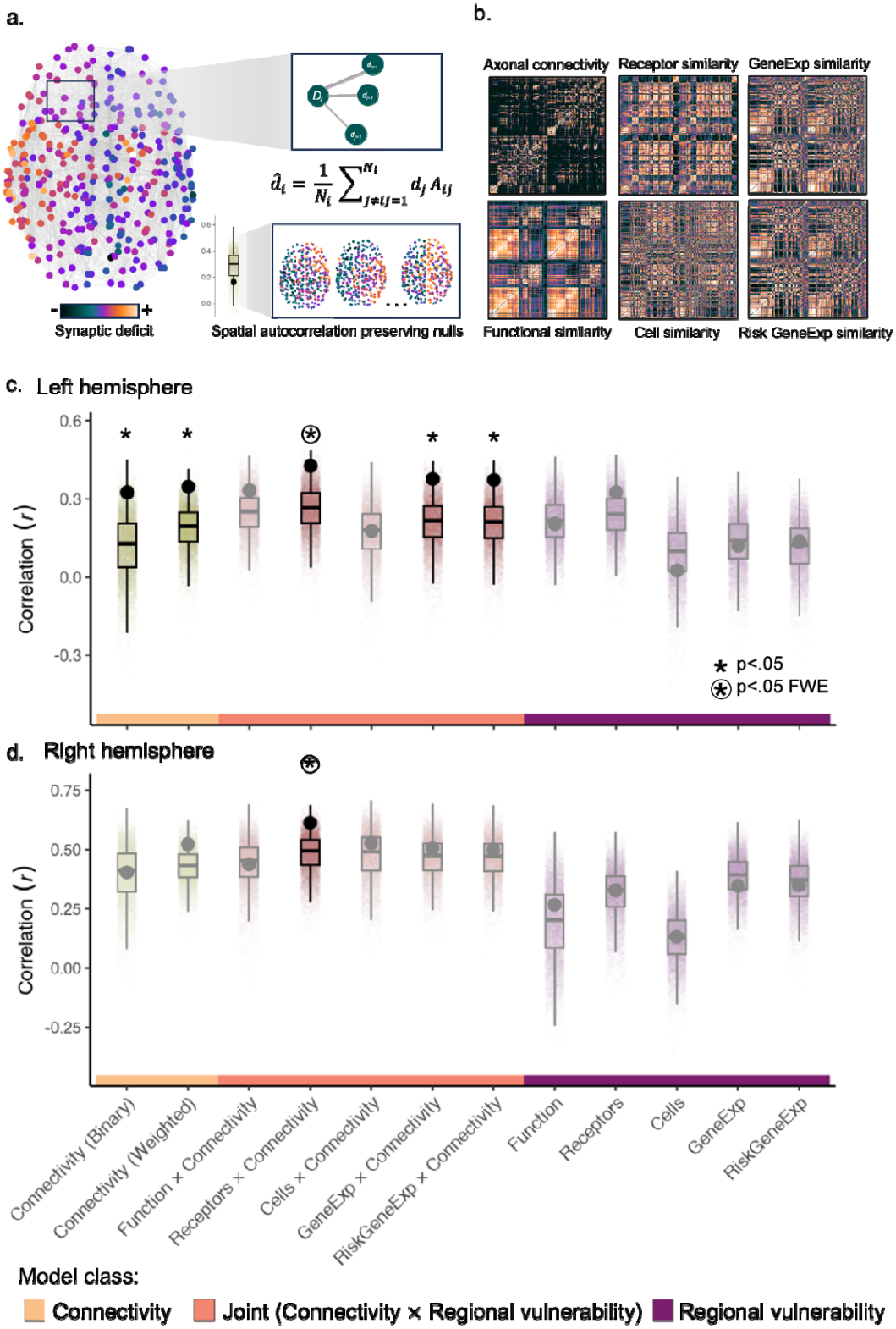

Fig 3. Synaptic pathology is constrained by global anatomical connectivity and local molecular vulnerability. a) Under the neighborhood deformation model, the estimated synaptic pathology of a node, D_i, is modelled as a weighted sum of the synaptic pathology values observed in its structurally connected neighbors, d_i. The weights are given by the adjacency matrix, A_{ij}. We tested 12 different neighborhood deformation models weighted by different combinations of feature similarity matrices. We compared each model performance to null models accounting for spatial autocorrelations in the synaptic pathology map. Models 1 and 2 assess the constraint of connectivity, with the first model denoted as Connectivity (Binary), in which $A_{ij} = 1$ if regions i and j share a connection and $A_{ij} = 0$ otherwise, and the second model, denoted as Connectivity (Weighted) in which the elements of A_{ij} correspond precisely to the weighted axonal connectivity matrix (**b**, top left) , such that the contribution of each neighbor is weighted by the strength of its connectivity to the index node. Models 3-7 assess the joint constrains of connectivity and feature similarity, by follow the same form as model 2, but weight the A_{ij} by one of the five feature similarity matrices **(b)**. Models 8-10 assess the constraint of feature similarity, removing the connectivity mask and considering all regions as neighbors to each index node, weighted by one of the five feature similarity matrices. GeneExp: Gene expression. **(c-d)** Black dots represent correlation between observed and neighborhood deformation model predicted synaptic deficit for right **(c)** and left **(d)** hemispheres, with colored dots representing null correlations. Asterisks (*) indicates statistical significance ($p<.05$), with a circle indicating survival against family-wise error correction (FWE).

Synaptic alterations propagate across axonally connected and molecularly similar regions

A close coupling between synaptic pathology and network-constrained chemoarchitecture implies that synaptic pathology may progressively spread through the connectome to molecularly similar regions. However, the previous neighborhood deformation models offer limited insight into the spatiotemporal dynamics of this process, nor is it able to identify regions from where pathology initiates. We therefore used a network diffusion model[69] to directly test whether synaptic loss propagates through the brain via a process of diffusion between axonally connected and molecularly similar regions (Fig 4A). Using a weighted combination of the group-consensus axonal connectivity and receptor/transporter similarity matrices (Fig 3C-D; `Receptors × Connectivity`) as a base, we simulated the spread of pathology by repeatedly initializing the model using each of the 332 regions as the starting seed, and for each iteration, estimating the diffusion of pathology at all other regions at 100 simulated timepoints. In this way, we were able to determine whether a diffusion process seeded from each region resulted in a spatial distribution of synaptic pathology that matched the empirically observed patterns. Consistent with prior work[22, 69], model performance was evaluated as the product-moment correlation between the predicted diffusion and observed synaptic abnormalities at each time step and for each seed, with the maximum correlation (r_{max}) across all time steps being retained.

The performance of the network diffusion model in capturing the empirical maps of synaptic pathology was compared to its performance in capturing surrogate maps generated using both a spatial autocorrelation-preserving null model and a network rewiring null model. The former null evaluated whether the observed findings were specific to the empirically observed pattern of synaptic alteration or were a generic property of the intrinsic spatial structure of the maps. The latter tests the hypothesis that any apparent network-based prediction of regional pathology is specific to the actual topology of the

network itself, and cannot be explained by basic network properties, such as regional variations in node degree or the spatial dependence of inter-regional connectivity and chemoarchitecture. FWE correction is applied to account for 332 seed regions. Further details regarding the network diffusion and benchmark null models can be found in the Methods.

Left inferior frontal areas were identified as the likely initiation site of synaptic pathology, showing the best performance and surviving FWE correction across both null models (r_{max}=.50; $p_{FWE} < .05$). The performance (r_{max}) for each brain region is shown in Fig 4B and statistically significant regions are shown in Fig 4C. Observed and predicted synaptic pathology maps using the best performing seed region are shown in Fig 4D. Overall, these finding suggest that synaptic pathology may initiate in inferior frontal regions in the left hemisphere and spread to molecular similar structurally connected regions.

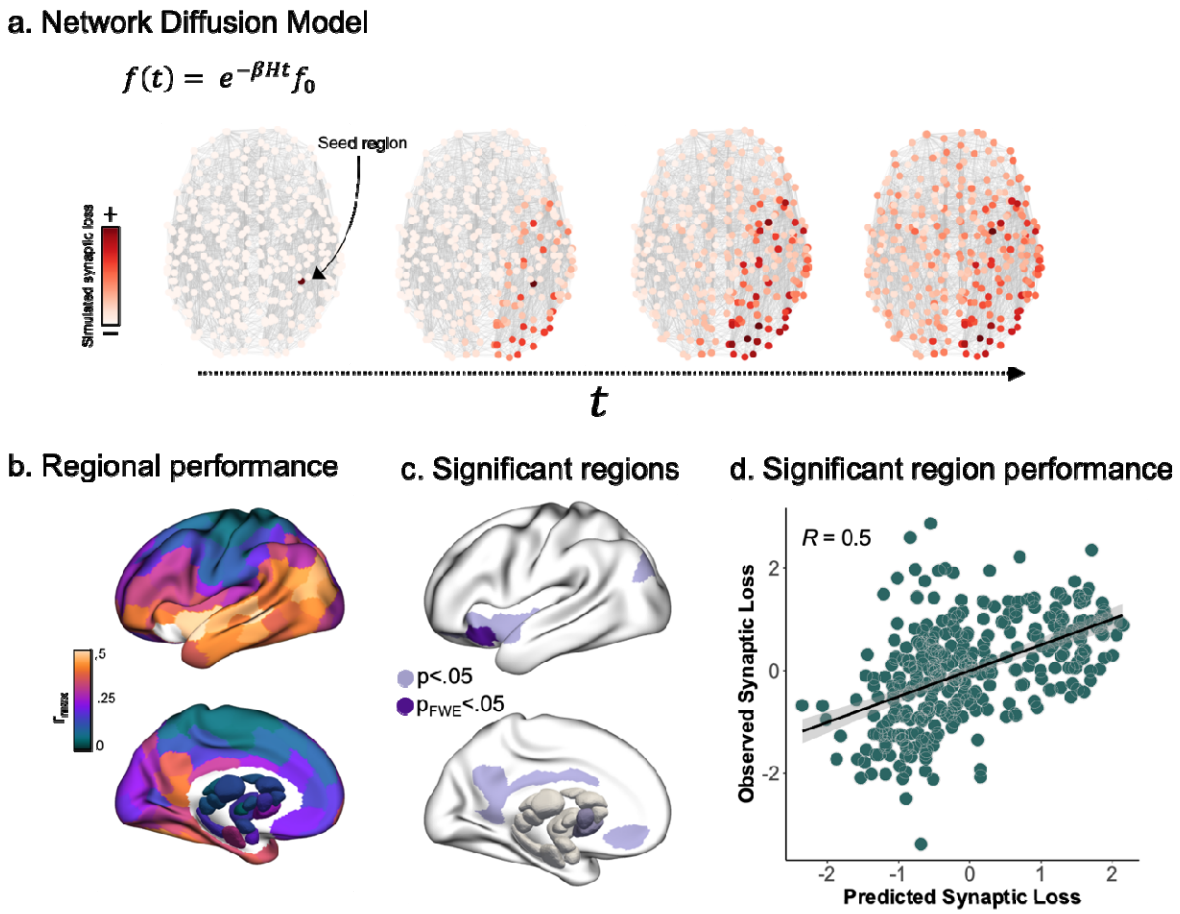

Fig 4. Spatiotemporal dynamics and initial sources of synaptic pathology. (a) To understand how global connectivity and local neurochemical vulnerabilities shape synaptic pathology, we simulated a spreading process using a network diffusion model. Using each of the 332 parcellated regions as a seed, we retained the maximum correlation between the simulated and observed synaptic abnormalities. We then compared maximum *r* values (r_{max}) for each region to a distribution of maximum *r* values from two benchmark null models accounting for spatial autocorrelations in the synaptic pathology maps and basic topological properties of the connectivity matrix (see Methods). **(b)** Model performance (r_{max}) for each region. **(c)** Seed regions with significantly greater r_{max} than both null models with light purple indicating $p<.05$ and dark purple indicating family-wise error corrected (FWE) $p<.05$. **(d)** Observed and network diffusion model predicted synaptic deficit, using the best performing seed (dark purple in **c**; left inferior frontal cortex).

Discussion

We show a brain-wide pattern of lower *in vivo* synaptic density in individuals with schizophrenia, compared to a large sample of healthy participants. Functionally defined frontoparietal/control areas were enriched for synaptic pathology, whereas limbic areas exhibited relatively less synaptic pathology. The magnitude of synaptic pathology is strongly coupled to the normative neurochemical composition, with areas rich in $GABA_{A/BZ}$, $5HT_{1B}$, $5HT_{2A}$, and $5HT_{6,}$ receptors, and lower in levels of CB_1 and $5HT_{1a}$ receptors most strongly affected. By testing competing network models we found regional synaptic pathology was predicted best by a model constrained by both axonal connectivity and neurochemical similarity, suggesting that local molecular properties interact with global connectivity to shape synaptic pathology in schizophrenia. Using simulation-based network diffusion models, left inferior frontal cortices were identified as initial sources from which synaptic pathology initiates and spreads to axonally connected and neurochemically similar areas.

Wide-spread lower synaptic density in schizophrenias

The quantification of synaptic density within the living brain used [^{11}C]UCB-J, a PET tracer that targets the Synaptic Vesicle Protein 2A (SV2A)[5, 70] which is localized and monodispersed on vesicular membranes within all chemical pre-synaptic boutons [71-73]. This tracer has highly specific binding to SV2A[74], good test-retest reliability[5, 75], and displacement within grey matter using a drug with specific binding to SV2A[5]. In primates, regional SV2A levels are strongly correlated (r >.95) with synaptophysin[5], a validated marker of *ex vivo* presynaptic density. Moreover, [^{11}C]UCB-J uptake recapitulates anatomically inferred patterns of synaptic density[5], has been shown to be sensitive to synaptic pathology across multiple neurodegenerative conditions[5, 76-78], and is specific to synaptic loss measured using electron microscopy, rather than reductions in protein levels[79]. Nonetheless, it is possible that the alterations detected here in schizophrenia represent reduced SV2A or vesicular organelles, in the absence of changes in terminal numbers. For instance, initial evidence suggested that a polymorphism in the SV2A gene may increase risk for schizophrenia, though this has not been replicated in recent large-scale genome-wise association studies[80]. Furthermore, while sustained vesicular depletion occurs as a secondary effect in neurological disorders initiated by illness-linked proteins[81-83], limited post-mortem evidence in schizophrenia actually suggests increased numbers and clustering of synaptic vesicles[84, 85]—findings that may result from *ex vivo* artifacts[86, 87].Given the sensitivity of [^{11}C]UCB-J to detecting synaptic terminal loss in other neurological conditions, and the strong converging genetic and post-mortem evidence demonstrating lower presynaptic terminals and dendritic spines in schizophrenia, it is likely that lower levels of [^{11}C]UCB-J binding detected here in schizophrenia are likely a result of lower numbers of synaptic terminals.

We find that areas of gray matter in individuals with schizophrenia, especially thalamic, striatal, hippocampal, frontal, temporal, cingulate, and occipital regions, show lower levels of synaptic density compared to controls, with medium to large effect sizes ($0.58 < d < 1.47$). These findings align with previous region-of-interest studies examining *in vivo* synaptic density in early psychosis and schizophrenia populations, which have reported lower tracer binding in frontal, anterior cingulate, hippocampal, temporal, occipital and striatal regions[7-10], using both measures of specific binding to SV2A,

such as that used in the current study, and measures that additionally index non-specific binding. Extending this prior work, our results suggest that synaptic alterations are not only isolated to these regions, but are more widespread, potentially impacting the totality of gray matter in chronic schizophrenia.

Patients with schizophrenia often exhibit alterations in gray matter volume[36-39, 42, 43], which can progressively worsen in some individuals[40, 41, 88]. Given the limited evidence from post-mortem studies for a reduction in the number of neurons, it has been theorized that the substrate underlying these MRI abnormities are alterations in synaptic, dendritic, and axonal organization[44]. However, there is limited direct evidence linking MRI signals to neurite changes in psychotic illnesses. Alternatively, MRI signal differences between patients and controls may reflect differences in properties related to myelination, soma, glia, vasculature, or extracellular space. The lack of neurobiological understanding behind MRI signal alterations in psychotic illness have led others to suggest that artefactual alterations between cases and controls in hydration, cholesterol levels, physical and mental activity, and stress[89-91] may be causes of the observed volumetric changes. Our finding that the pattern of synaptic and gray matter alterations does not spatially correlate within the same or independent samples across different stages of illness suggests that a lowering of presynaptic terminals is not the primary substrate underlying gray matter MRI abnormalities in psychotic illness. This finding is also consistent with prior work demonstrating that age-related loss of synaptic density has a different spatial pattern to age-related MRI-derived gray matter volume loss[92]. Although, future work should examine association with a broader range of MRI-derived gray matter metrics such as cortical thickness and surface area.

Local molecular vulnerability and global axonal connectivity jointly shape synaptic abnormalities

In many neurological illnesses, pathological processes selectively target or initiate from specific genetic, cellular[93, 94], neurochemical[95, 96], and functional systems[18, 97]. Here, we find evidence for the preferential accumulation of synaptic pathology within functionally defined control systems, specifically dorsal precuneus and posterior cingulate areas. This is consistent with a large body of work demonstrating that higher-order transmodal association areas are a primary site of pathology in psychosis[98]. Our findings also indicate a strong spatial correspondence of synaptic pathology with normative receptor profiles. Specifically, regions typically rich in $GABA_{A/BZ}$, $5HT_{1B}$, $5HT_{2A}$, and $5HT_{6,}$ receptors, and lower in levels of CB_1 and $5HT_{1a}$ receptors, show vulnerability to synaptic pathology. All three receptor systems have been shown to be disrupted or track symptom severity in schizophrenia[99-102], suggesting that synapses associated with these systems are vulnerable to pathology. This is also consistent with genetic findings showing that enrichment of common variant associations is restricted to genes that are expressed in both excitatory and inhibitory neurons[103, 104] and in genes encoding proteins involved in general synaptic features. We did not find that densities of transcriptomically-defined cell types were predictive of the spatial pattern of synaptic pathology. Many post-mortem and genetic studies have shown layer specific cell abnormalities, commonly in frontal supragranular cells[105, 106] and particularly in cortical layer three[2, 46, 107]. The current spatial resolution of PET does not allow for layer specific inference, therefore a spatial correspondence with layer specific cell types may become apparent with improving resolutions.

In addition to regional molecular vulnerabilities, we find that the axonal connectivity, indexed using high-resolution diffusion MRI, constrains synaptic alterations. Specifically, regional predictions of synaptic

pathology constrained by axonal connectivity and weighted by inter-regional receptor/transporter similarity showed superior performance to models constrained by connectivity alone, or weighted by a range of other neural properties. This finding demonstrates that local neurochemical vulnerabilities interact with the global axonal topology of the brain to shape pathology. Similar findings have been demonstrated in other neurological conditions such as Parkinson's disease[28] and frontotemporal dementia[108], where pathology depends on local regional properties and manifests in a manner consistent with macro-scale axonal topology. In schizophrenia, anatomical alterations in patients are often correlated across spatially distributed regions[63-66], corresponding with normative connectome organization[67, 68], and are consistent with network-based spreading constrained by axonal connectivity[22, 24]. Our results suggest that the spatial pattern of synaptic alterations in schizophrenia is a result of both regional molecular vulnerabilities and global connectivity, rather than either one of these neural features in isolation.

The strong link between synaptic alterations and network chemoarchitecture suggests that pathology may spread across the connectome to regions with similar molecular features. We used a network diffusion model to understand the spatiotemporal dynamics underlying the molecular and connectivity constraints. We find that left inferior frontal regions are a putative initial source of synaptic density loss in schizophrenia. Neuroanatomical alterations in these regions are some of the earliest neural alterations reported in the initial stages of illness[109-111], and overlap with putative sources of longitudinal gray matter loss previously identified in unmedicated first episode psychosis samples[22]. This is also consistent with recent large-scale studies that have subtyped schizophrenia based on the trajectory of gray matter changes, which found that the largest subtype is characterized by initiation of pathology in inferior fronto-insular areas.[112, 113]. Our results are in line with a spreading process in which pathological processes preferentially propagate via axonal connections to molecularly similar areas. The precise mechanism driving this process remains unclear. Trans-neuronal spreading processes have often been seen in prion-like spread of misfolded proteins, but limited evidence exists for visible deposits of aggregated pathological proteins in psychotic illness (although see[114-116]). However, although speculative, subtle changes in protein homeostasis[16] may interact with regional neurotransmitter levels[117, 118] and spread to synaptically connected distal brain region[119, 120]. Alternatively, and given the commonly reported finding of functional brain alterations in psychotic disorders, dysfunction of one region may trigger abnormal functional activity in connected sites that, over time, may trigger synaptic changes as a result of aberrant neurotransmission or a loss of trophic support[21]. Indeed, the trans-neuronal propagation of glutamate-mediated excitotoxicity may account for lower synaptic density reported in schizophrenia[14].

One of the more prominent hypotheses regarding synaptic pathology in schizophrenia implicates the immune-mediated complement component 4 (C4) protein of the major histocompatibility complex, and other complement cascade proteins, in microglial-mediated synaptic pruning. Of relevance to the current findings, neurotransmitter homeostasis has also been shown to mediate this process, with excessive release of glutamate activating extra-synaptic glutamatergic receptors in microglia, leading to microglial activation via reactive oxygen species, release of ATP and cytokines, which in turn results in synaptic dysfunction and loss[121]. Importantly, other risk factors for schizophrenia may also lead to microglial activation, such as cannabis use[122] and psychosocial stress[123].

This study has some limitations. Our analysis of synaptic density depended on group-level summary values and may not directly reflect synaptic differences for individual patients. While the extent of

interpatient heterogeneity in synaptic pathology is currently unknown, subsequent work could use larger samples with synaptic density imaging to derive patient-specific measures, such as those obtained through normative modelling[124, 125]. The cross-sectional nature of this study precludes inference about the temporal onset of synaptic pathology, and further longitudinal studies will be able to clarify whether these alterations occur during neurodevelopment, at transition to illness or at later stages. An important consideration here is that the cell and receptor density maps used in the current study were derived from healthy samples and therefore represent normative cytoarchitecture and chemoarchitecture. Future data aggregation efforts examining cell-type and receptor maps from patient populations may provide additional evidence regarding synaptic vulnerabilities in schizophrenia. Our approach to characterize structural connectivity is also limited by the accuracy of diffusion MRI[126]. While the processing procedures we applied enhanced the biological validity of our structural connectivity measures as much as possible[127], further developments in non-invasive connectivity mapping and tractography will be required to allow more precise mechanistic inferences about constrains imposed by axonal pathways.

Overall, our findings provide *in vivo* evidence of widespread lower synaptic density in schizophrenia that is jointly constrained by axonal connectivity and molecular similarity between regions. Moreover, we find that synaptic pathology may initiate in prefrontal areas and spread to axonally connected and molecularly similar areas.

Acknowledgements and Disclosures

SC is supported by the American Australian Association and the University of Melbourne McKenzie Fellowship. IE (Nancy Taylor Foundation and VA NCPTSD), DM (NINDS R01NS124819)).AS is supported by the Yale Wu Tsai Postdoctoral Fellowship). VC is supported by an Australian NHMRC Investigator Grant (1177370) and a University of Melbourne Dame Kate Campbell Fellowship. This study was supported in part by the National Institute on Drug Abuse (NIDA) grant R01 DA052454-03 (GAA), U54 AA027989 (KC), Dana Foundation David Mahoney program (RR), CTSA Grant Number UL1 TR001863 from the National Center for Advancing Translational Science (NCATS) (RR), National Center for Homelessness among Veterans (36C24820Q1276) (RR). We also thank Dr. Jack Tsai (NCHAV) for administrative support.

Methods

Sample characteristics

A total of 122 individuals, including 29 individuals diagnosed with schizophrenia were included in this study. Individuals with schizophrenia were recruited via clinician referrals, paper, and web advertisements. The majority of individuals with schizophrenia were recruited using criteria that excluded based on the following criteria: regular exposure to drugs of abuse (except nicotine and caffeine) within the past 3 months based on history or positive urine drug screen, lifetime substance use disorder (except for nicotine and caffeine), weekly alcohol consumption exceeding National Institute on Alcohol Abuse and Alcoholism (NIAAA) guidelines (4 or more drinks on any single day and/or 21 or more drinks per week for males), history of significant head injury resulting in unconsciousness, unstable medical condition, significant prior exposure to radiation, metal in the body which would exclude MRI scan or claustrophobia. A subset of individuals with schizophrenia were recruited using a less restrictive criteria, where substance use was not an exclusion. We repeated our primary analyses after excluding subjects with a history of, or current, substance abuse (n=7; SFig1). Data from 13 of the included individuals with schizophrenia have been part of a previously published study[9]. The healthy control subjects were included from studies performed at the Yale PET Center using the [^{11}C]UCB-J PET to investigate brain synaptic density across a variety of neuropsychiatric conditions. Healthy control individuals were excluded for a current and/or lifetime diagnosis of a psychiatric disorder, current or past serious medical or neurological illness (including a history of head injury with loss of consciousness), metal in body which would result in MRI contraindication, or a history of substance abuse or dependence. Demographic and sample characteristics are provided in Table 1. All study protocols were approved by the Yale University Human Investigation Committee and Radiation Safety Committee. All participants provided written informed consent prior to participation.

PET and MR imaging acquisition and processing

[^{11}C]UCB-J was synthesized using established methods[74]. All [^{11}C]UCB-J PET measurements were conducted on the HRRT (Siemens Medical Solutions), which acquires 207 slices (1.2-mm slice separation) with a reconstructed image resolution (full width at half maximum) of ~3 mm. Before every [11C]UCB-J injection, a transmission scan was performed for attenuation correction. Dynamic PET data (frames: 6 × 0.5 min, 3 × 1 min, 2 × 2 min, and 10 × 5 min) were acquired and reconstructed using the MOLAR algorithm[128]. Event-by-event motion correction was performed using Polaris Vicra optical tracking (NDI Systems, Waterloo, Canada) with reflectors mounted on the subject's head via a swim cap[129]. All gray matter voxels were corrected for partial volume effects using the Müller-Gärtner algorithm[130]. Then, the simplified reference tissue model 2 (SRTM2)[131, 132] with the centrum semiovale as the reference region, was applied using 60 mins of dynamic data to generate parametric images of binding potential (BP_{ND}) [5, 9, 33, 35]. Mean voxel-level BP_{ND} maps for patients and controls are provided in SFig. 2)

A high-resolution T1-weighted structural MPRAGE scan (TR/ TE = 2530/3.34, flip angle = 7°, in-plane resolution = 0.98 × 0.98 mm, matrix size = 256 × 256, slice thickness = 1 mm, slices = 176) was acquired on a 3T MAGNETOM Prismafit scanner (Siemens, Erlangen, Germany) for image registration. Registration of parametric PET images to Montreal Neurological Institute (MNI152) standard space was performed using SPM12 (Wellcome Trust center for Neuroimaging, London, UK)[133]. For each subject,

PET images were motion-corrected by registering each frame to a summed image (0–10 min post-injection). A linear registration aligned the summed PET image to the T1-weighted MR image, followed by a nonlinear registration to the MNI template. The combined transformations were then applied to the parametric PET image. The standardized parametric PET images were smoothed with a 4mm full width half maximum Gaussian kernel then masked using an enhanced gray-matter tissue prior map thresholded at .25[134].

Quantifying synaptic density alterations

General liner models examining lower BP_{ND} in individuals with schizophrenia compared to controls, while adjusting for age and sex, were fit at each of approximately 500,000 grey matter voxels. Non-parametric voxel-level family-wise error (FWE) correction was implemented using CAT12[135], using 5000 permutations, with significance assessed at $p_{FWE} < .0.05$ (Fig1A).

Association between grey-matter volume and synaptic density alterations

Voxel-based morphometry (VBM), implemented in the CAT12 toolbox[135], was used to index brain-wise grey matter volume alteration between individuals with schizophrenia and controls within the current sample, as well as four previously published independent samples[22] which included individuals with medication-naive first-episode psychosis[41] ($N_{case/control}$=59/27), early psychosis[47] ($N_{case/control}$=121/57), and two cohorts of established schizophrenia[48, 49] ($N_{case/control}$=66/72; $N_{case/control}$=70/62). The VBM procedure used for each sample has been previously described in detail[22]. The resulting brain-wide voxel-level t-statistic map from each study, which indexed differences in gray matter volume between patients and controls, were then parcellated into 300 discrete cortical[50] and 32 subcortical[51] areas of approximately equal size, using previously validated atlases. The volume alteration of a region was estimated as the mean test-statistic (comparing patients and controls) of all voxels corresponding to that region. The same parcellation procedure was followed for synaptic density alteration map from the current sample (Fig 1B), allowing for direct comparison between synaptic and gray-matter volume alteration maps. Product-moment correlations (r) were used to examine spatial associations between synaptic density alteration and gray matter alterations within the current sample and four independent samples (Fig 1C). Statistical significance of associations between spatial maps was assessed using a benchmark null model that preserved spatial autocorrelation, allowing us to evaluate whether the observed findings were specific to the empirically observed alteration maps or were a generic property of the intrinsic spatial structure of these maps. The procedure used a spin-test to rotate cortical region-level t-values from the synaptic density alteration map 10,000 times[52, 53]. The rotation was applied to one hemisphere and then mirrored for the other hemisphere. Sub-cortical t-values were randomly permuted within one hemisphere and then mirrored for the other hemisphere. All *p*-values were quantified as the fraction of null correlation values exceeding the observed correlation, considering both positive and negative tails of the null distribution (two-tailed). Statistical significance was assessed at $p<.05$ and inference was FWE corrected using a maximum-statistic method (Fig 1C).

Quantifying network, neurochemical and cellular enrichment of *synaptic density alterations*

Network-level enrichment. To examine whether synaptic density alterations were preferentially enriched within specific large-scale canonical functional networks and cytoarchitectonic territories, we used two brain system classifications: i) intrinsic functional networks based on the 17 cortical Yeo[50, 55] and 3 subcortical Tian[51] classifications and ii) cytoarchitectonic types of laminar differentiation based on the

canonical von Economo and Koskinas atlas [52, 57, 136]. Classifications for the cytoarchitectonic subdivision of each of the 332 regions was determined using the previously published Schaefer et al characterization for intrinsic functional networks, and was assigned according to established classifer[136] which generated vertex-level network classifications, which were converted into parcel-level assignments using a the winner-take-all approach[52]. Synaptic pathology was estimated averaging the t-statistic across regions belonging to each functional network or cytoarchitectonic subdivision (Fig. 2A-B). Statistical significance of observed systems-level synaptic pathology was compared to mean values derived using the spin-test with 10,000 permutations, as previously described. Statistical inference was assessed at $p<.05$ (two-tailed) and FWE corrected using the maximum statistic method. For each network, we computed z-scores by comparing the observed effect size to the null distribution.

Neurochemical and cellular associations. To examine whether synaptic density alterations were preferentially enriched with normative neurochemical or cellular densities, we used two sources of data. For regional normative neurochemical densities, we used 24 different group-consensus PET binding maps from healthy population collated by the *neuromaps* toolbox[58]. Following previous work, for tracers that had multiple samples, a sample-size weighted average map was computed[137]. Further details regarding each PET map are provided elsewhere[58]. Each PET map was masked and parcellated into the same 332 region atlas as the synaptic density alteration maps and mask. Regional transcriptomic cell-type concentrations were deconvolved from whole brain bulk tissue transcriptions provided by the Allens Human Brain Atlas (AHBA)[61], with 24 different cell-types being imputed using recently published single-nucleus RNA-sequencing data[59] (see Zhang et al[60] for detailed overview). Briefly, the transcription signatures identifying each class of cell in the AHBA bulk samples were derived from cortical single-nucleus RNA sequencing (snRNA-seq) data of eight cortical areas. This included 24 cellular classes with distinct laminar specialization, developmental origin, morphology, spiking pattern, and broad projection targets[138]. These cells include 9 GABAergic inhibitory interneurons (PAX6, SNCG, VIP, LAMP5, LAMP5 LHX6, Chandelier, PVALB, SST CHODL, SST), 9 glutamatergic excitatory neurons (L2/3 IT, L4 IT, L5 IT, L6 IT, L5 ET, L5/6 NP, L6 CT, L6b, L6 IT Car3), and 6 non-neuronal cells (Astro, Endo, VLMC, Oligo, OPC, Micro/PVM). This procedure resulted in cell density estimates for each of the 24 cell-types at each cortical region using the same atlas as the synaptic density alteration maps. Due to data availability, non-cortical areas were excluded for analyses that used these cellular data.

Given that regional neurochemical and cellular profiles are multivariate, we examined enrichment between each of these two features and synaptic density alterations using robust non-parametric canonical correlation analyses[62]. Two canonical correlation analyses models were computed, examining the associations between regional synaptic density alterations and receptor (Fig. 2C) or cell densities (SFig5). Statistical significance of the observed canonical correlations (r_{cca}) compared to null correlations derived using the spin-test with 10,000 permutations. Statistical inference was assessed at $p<.05$ (two-tailed). To examine which cell or receptor/transporter maps contributed most to synaptic density alterations, we quantified canonical loadings by computing product moment correlations between the 24 input maps and corresponding canonical variate. To assess statistical significance of canonical loadings, we used robust bootstrapping to estimate the standard error for each input map, computed z-scores by dividing the correlation by the standard error and used these z-scores to compute two-tailed p-values[139]. Maps showing reliable loadings on the canonical variate were those that survived a Bonferroni FWE-correction of these values ($p < .05$; two-tailed; Fig 2D).

Neighborhood Deformation Model

Normative feature similarity networks

Structural connectivity. To estimate inter-regional axonal connectivity, we computed a representative weighted connectivity matrix from tractography applied to diffusion-weighted imaging (DWI) data from an independent healthy unrelated cohort of 150 (71 males, aged 21-35 years) individuals from the from the S900 release of the Human Connectome Project[140], which served as a reference connectome for computational modelling. This subset of 150 individuals was selected to reduce computational burden, and represented individuals with the lowest head motion, as estimated using framewise displacement[141]. Data were acquired on a customized Siemens 3T Connectome Skyra scanner at Washington University in St. Louis, MO, USA, using a multishell protocol for the diffusion weighted imaging with the following parameters: 1.25-mm^3 voxel size; repetition time = 5520 ms; echo time = 89.5 ms; field of view of 210 mm by 180 mm; 270 directions with b = 1000, 2000, 3000 s/mm^2 (90 per b value); and 18 b = 03 volumes. Structural T1-weighted data were acquired with 0.7 mm voxels, repetition time = 2400 ms, echo time = 2.14 ms, and a field of view of 224 mm^2.

The DWI data first underwent the HCP minimal pre-processing pipeline[142], that included normalization of mean b = 0 images across diffusion acquisitions and correction for echo-planar imaging susceptibility and signal outliers, eddy current–induced distortions, slice dropouts, gradient nonlinearities, and participant motion. T1-weighted data were corrected for gradient and readout distortions before being processed with FreeSurfer[143]. Further details regarding this pipeline are provided elsewhere[144]. Using the corrected DWI data, fiber orientation distributions were estimated using multishell Constrained Spherical Deconvolution[145]. Probabilistic tracking was performed with the Fiber Orientation Distributions (iFOD2) algorithm, implemented using MRtrix3[146, 147] and used Anatomically Constrained Tractography which takes advantage of previously computed tissue maps to ensure that that streamline can begin, traverse, and terminate in anatomically plausible locations[148]. A total of 10 million streamlines were generated using dynamic seeding along with default MRtrix3 parameters[146, 149]. The same 332 regions atlas used to parcellate the synaptic density alteration map[50, 51] was then transformed from template surface space to the individual surface of each subject using the spherical registration[150]. Next, the parcellation was projected to a volumetric image and resampled to the same resolution as the DWI using nearest-neighbor interpolation[151]. To create a connectivity matrix, streamlines were assigned to each of the closest regions in the parcellation within a 5mm radius of the streamline endpoints[146].

Importantly, most tractography algorithms are prone to false positives and do not directly index the quantitative strength of connections between pairs of regions[126, 152]. We therefore implemented a state-of-the-art optimization procedure, Convex Optimization Modelling for Microstructure Informed Tractography (COMMIT2), which has shown to be superior to other methods on key benchmarks derived from fiber-tracking phantoms[127]. COMMIT2 uses a forward model to recover the connectivity matrix with the minimum number of bundles that best explains the local axon density estimated from the DWI signal[127]. In doing so, the algorithm filters and re-weights inter-regional connectivity strengths and provides more biologically accurate quantitative estimates of connectivity. After optimized connectivity matrices were generated for each subject, we computed a single group-consensus matrix by retaining connections if they appeared in at least τ subjects, where τ is the consensus threshold that results in a binary density comparable to that of a typical subject[153], and which was set to 37.7% for this sample. This threshold is computed separately for inter-/intra-hemispheric connections. Retained connections are

assigned the corresponding group-average connectivity weight, resulting in a weighted consensus connectivity matrix. Finally, the connectivity weights from the group- consensus matrix were z-scored. This procedure resulted in a single 332 × 332 weighted connectivity matrix (Fig3B).

Functional similarity. To estimate inter-regional similarity of hemodynamic fluctuations, often referred to as functional connectivity, we used resting-state functional MRI data from the same 150 subjects from the Human Connectome Project described above (see Structural connectivity). All rs-fMRI data were obtained using a 32-channel Siemens 3T connectome-Skyra scanner. The imaging parameters for rs-fMRI were as follows: repetition time=720□ms, echo time=33.1□ms, flip angle=52°, field of view=208□×□180□mm^2, matrix=104□×□90, slice number=72, slice thickness=2□mm, voxel size=2 mm^3, multiband factor=8 and 1,200 volumes. Participants were required to stay awake, relaxed and to keep their eyes open and fixed on a bright crosshair projected on a dark background. A detailed description of the Human Connectome Project data acquisition procedures is available elsewhere[140]. Using data from the first run (left to right phase encoding direction), the Human Connectome Project minimal preprocessing pipeline was applied, which includes gradient-nonlinearity-induced distortion, motion correction to the single-band reference image[151], distortion correction[154], registration into template space using a boundary-based-registration algorithm and single-step spline interpolation using all transforms, intensity normalization and bias field removal. After minimal high-pass filtering with a cutoff of 2,000ms, independent component analysis X-noiseifier (ICA-FIX)[155] was applied using pre-trained Human Connectome Project classifier. Next, the volume time series were mapped into the standard CIFTI grayordinate space and smoothed to 2 mm full width at half maximum. Further details regarding the processing and denoising has previously been described in detail[125]. We then parcellated each individual's normalized and denoised scans into the same 332 regions atlas used to parcellate the synaptic density alteration map[50, 51]. Inter-regional functional similarity was estimated as the as the zero-lag product moment correlation between each pair of regional time series for each individual. Finally, the individual correlation matrices were fishers z-transformed and single group-consensus mean matrix was derived across the sample, resulting in a single 332 × 332 weighted similarity matrix (Fig. 3B).

Receptor/transporter similarity. Inter-regional receptor and transporter similarity were estimated using the same parcellated 24 PET binding maps described above (see *Neurochemical and cellular enrichment)* Regional binding values were then z-scored within each map and product moment correlations were computed between each region's receptor/transporter profile. Finally, the resulting correlation matrix was Fishers z-transformed, resulting in a single 332 × 332 weighted similarity matrix (Fig. 3B).

Cell-type similarity. Inter-regional cell-type similarity was estimated using cortical regional density maps for 24 transcriptomic cell-types described above (see *Neurochemical and cellular enrichment*). Regional density values were then z-scored within each map and product moment correlations were computed between each region's cell-type density profile. Finally, the resulting correlation matrix was Fishers z-transformed, resulting in a single 300 × 300 weighted similarity matrix (Fig. 3B).

Gene expression similarity. Inter-regional transcriptomic similarity was estimated using whole brain bulk tissue transcriptions provided by the Allens Human Brain Atlas[61], processed using the *abagen* toolbox[156, 157]. Regional microarray expression data were obtained from 6 post-mortem brains (1 female, ages 24.0--57.0, 42.50 +/- 13.38) provided by the Allen Human Brain Atlas (AHBA, https://human.brain-map.org;

[H2012N]). Data were processed with the abagen toolbox (version 0.1.4+15.gdc4a007; https://github.com/rmarkello/abagen; [156]) using a 332-region volumetric atlas in MNI space.
First, microarray probes were reannotated previous data[157]; probes not matched to a valid Entrez ID were discarded. Next, probes were filtered based on their expression intensity relative to background noise[158], such that probes with intensity less than the background in >=50.00% of samples across donors were discarded. When multiple probes indexed the expression of the same gene we selected and used the probe with the highest mean intensity across samples. The selection of probes was performed using sample expression data aggregated across all donors. The MNI coordinates of tissue samples were updated to those generated via non-linear registration using the Advanced Normalization Tools (ANTs; https://github.com/chrisfilo/alleninf). Samples were assigned to brain regions in the provided atlas if their MNI coordinates were within 2 mm of a given parcel. To reduce the potential for misassignment, sample-to-region matching was constrained by hemisphere and gross structural divisions (i.e., cortex, subcortex/brainstem, and cerebellum, such that e.g., a sample in the left cortex could only be assigned to an atlas parcel in the left cortex[157]). If a brain region was not assigned a sample from any donor based on the above procedure, the tissue sample closest to the centroid of that parcel was identified independently for each donor. The average of these samples was taken across donors, weighted by the distance between the parcel centroid and the sample, to obtain an estimate of the parcellated expression values for the missing region. All tissue samples not assigned to a brain region in the provided atlas were discarded.
Inter-subject variation was addressed by normalizing tissue sample expression values across genes using a robust sigmoid function[159]:

$$x_{norm} = \frac{1}{1 + \exp(-\frac{(x - \langle x \rangle)}{\mathrm{IQR}_x})}$$

where $\langle x \rangle$ is the median and IQR_x is the normalized interquartile range of the expression of a single tissue sample across genes. Normalized expression values were then rescaled to the unit interval:

$$x_{scaled} = \frac{x_{norm} - \min(x_{norm})}{\max(x_{norm}) - \min(x_{norm})}$$

Gene expression values were then normalized across tissue samples using an identical procedure. Samples assigned to the same brain region were averaged separately for each donor and then across donors, yielding a regional expression matrix. Product moment correlations were computed between each region's gene expression profile. Finally, the resulting correlation matrix was Fishers z-transformed, resulting in a single 332 × 332 weighted matrix (Fig. 3B).

Risk gene expression similarity. To generate a gene expression similarity matrix from a restricted set of genes implicated in schizophrenia, we used a previously published curated set of 120 genes that were prioritized based on a triangulation of population genetic and ex vivo methods. Of these genes, the expression of 92 genes passed the quality control procedures described above for the AHBA data and were used to generate a risk gene similarity matrix. Product moment correlations were computed between each region's risk gene expression profile. Finally, the resulting correlation matrix was Fishers z-transformed, resulting in a single 332 × 332 weighted matrix (Fig3B).

Model Specification

We evaluated the contributions of connectivity and regional vulnerabilities on synaptic density using the Neighborhood Deformation Model[24] . The model is given by

$$\hat{d}_i = \frac{1}{N_i} \sum_{j=1, j \neq i}^{N_i} d_j A_{ij} \ ,$$

where $\hat{d}_i$ is the predicted synaptic density alteration in region i, N_i is the number of connected neighbours of i, d_j is the alteration observed in the j-th neighbour of region i, and A_{ij} defines the connectivity between regions i and j.

Twelve different matrices were substituted for A_{ij}, yielding 12 variants of the neighborhood deformation model. All matrices were min/max transformed to values between [0,1] to remove negative values. These models fell into three broad classes that assess the contribution of connectivity, regional vulnerability, or a combination of these constraints, on synaptic pathology. The models were parameterized as follows:

Models 1 and 2 follow similar forms to previously used neighborhood deformation models[22, 24], and tested the constraint of connectivity. In Model 1, denoted Connectivity (Binary), A_{ij}=1 if region i and j are connected in the group-consensus structural connectivity matrix and zero otherwise. Therefore, all j structurally connected neighbours make an equal contribution to predicting the extent of synaptic pathology observed in region i. In Model 2, denoted Connectivity (Weighted), A_{ij} corresponded to the weighted structural connectivity matrix. Therefore, this models, the contributions of region i's neighbours were weighted by inter-regional structural connectivity estimates, such that neighbours of node i with a more strongly weighted connection made a stronger contribution to predicting regions i's synaptic pathology (Fig3A).

Models 3 to 7 tested the joint constraint of connectivity and regional vulnerabilities. In these models A_{ij} corresponded to the connectivity matrix weighted by one of five feature similarity matrices: function, receptor/transporter expression, cell type abundance, gene expression, and schizophrenia-related risk gene expression (Fig3B). These models are denoted by the feature name '× connectivity' (Fig. 3C-D). In all five models, only edges that had a corresponding structural connection were included and edge weights were taken from feature similarity matrices.

Models 8 to 12 test the impact of regional vulnerabilities alone by removing the constraint of structural connections. In these models A_{ij} corresponded to one of five feature similarity matrices: function, receptor/transporter expression, cell type abundance, gene expression, and schizophrenia-related risk gene expression (Fig. 3B). These models are denoted by the feature name (Fig. 3C-D). In all five models, all edges that were included and edge weights were taken from feature similarity matrices.

Neighborhood deformation model evaluation

Neighborhood deformation model performance was evaluated with the product-moment correlation (r) between estimates of observed and predicted synaptic pathology (Fig 3A). To assess statistical significance, we compared the performance of each model to benchmark null models via a spin-test with 10,000 permutations, which evaluated whether the observed findings were specific to the empirically observed pattern of synaptic pathology or were a generic property of the intrinsic spatial correlation structure of this map. Statistical inference was assessed at p<.05 (two-tailed) and FWE corrected using the maximum statistic method. see *Association between grey-matter volume and synaptic density alterations* for further details about benchmark null models.

Network diffusion model

The previous neighborhood deformation models evaluate the degree to which the spatial pattern of synaptic pathology is shaped by global connectivity and regional properties. A close coupling between synaptic pathology and molecular network architecture implies that synaptic density loss may spread through the connectome, but the models offers limited insight into the dynamics of the spreading process, nor is it able to identify regions from where the pathology initiate. We therefore used a network diffusion model to directly test whether synaptic density loss spreads through the brain via a process of diffusion and whether certain brain regions act as sources, or initiation sites, of pathological spread through the brain (Fig4)[69]. The network diffusion model simulates the dynamic spread of pathology between the nodes of a weighted network via a process of diffusion (Fig4A), defined as

$$f(t) = e^{-\alpha H t} f_0 \,,$$

where t is the model diffusion time, which has arbitrary units (a.u.), and $f(t)$ is a vector characterizing the amount of diffusion in each region at time t. Based on the results of the previous neighborhood deformation modelling, we the receptor/transporter similarity matrix, constrained by the structural connectivity matrix, as the base of diffusion modelling. The strength of the diffusion process is controlled by a constant (α) and H is the Laplacian of the weighted base matrix. f_0 represents the initial distribution of pathology. We repeatedly initialized the model using each of the 332 regions as the starting seed, such that the initial state was set to 1 for the seed region, and 0 for all other regions. At each initialization, using a constant of $\alpha = 1$, the network diffusion model was used to estimate the diffusion at all other regions at time $t = 0$ to 50. In this way, we were able to determine whether a diffusion process seeded from each region resulted in a spatial distribution of synaptic density loss that matched the empirically observed patterns.

Network diffusion model evaluation

Consistent with prior work[22, 69, 160], model performance was evaluated as the product-moment correlation between the predicted diffusion and observed volume abnormalities at each time step and for each seed, with the maximum correlation (Fig4B; r_{max}) across all time steps being retained. The seed region was excluded when correlating predicted and observed volume abnormalities to ensure that our analysis was not influenced by large volume abnormalities in the seeds. The performance of the NDM in capturing the empirical maps of GMV change was compared to its performance in capturing surrogate maps generated using the $\text{Null}_{\text{smash}}$ and $\text{Null}_{\text{rewire}}$ benchmark models (Fig4A). The $\text{Null}_{\text{spin}}$ benchmark was not used to

evaluate the NDM as it does not include subcortical regions. Further details about benchmark null models used to evaluate the NDM can be found in the Supplement.

References

1. Osimo, E.F., Beck, K., Reis Marques, T. & Howes, O.D. Synaptic loss in schizophrenia: a meta-analysis and systematic review of synaptic protein and mRNA measures. *Molecular Psychiatry* **24**, 549-561 (2019).
2. Berlekom, A., *et al.* Synapse Pathology in Schizophrenia: A Meta-analysis of Postsynaptic Elements in Postmortem Brain Studies. *Schizophr Bull* **46**, 374-386 (2020).
3. Sekar, A., *et al.* Schizophrenia risk from complex variation of complement component 4. *Nature* **530**, 177-183 (2016).
4. Fromer, M., *et al.* De novo mutations in schizophrenia implicate synaptic networks. *Nature* **506**, 179-184 (2014).
5. Finnema, S.J., *et al.* Imaging synaptic density in the living human brain. *Science translational medicine* **8**, 348ra396-348ra396 (2016).
6. Husain, M.O., *et al.* A systematic review and meta-analysis of neuroimaging studies examining synaptic density in individuals with psychotic spectrum disorders. *BMC psychiatry* **24**, 460 (2024).
7. Yoon, J.H., *et al.* Reductions in synaptic marker SV2A in early-course Schizophrenia. *Journal of Psychiatric Research* (2023).
8. Onwordi, E.C., *et al.* Synaptic terminal density early in the course of schizophrenia: An in vivo UCB-J positron emission tomographic imaging study of SV2A. *Biological psychiatry* **95**, 639-646 (2024).
9. Radhakrishnan, R., *et al.* In vivo evidence of lower synaptic vesicle density in schizophrenia. *Molecular Psychiatry* (2021).
10. Onwordi, E.C., *et al.* Synaptic density marker SV2A is reduced in schizophrenia patients and unaffected by antipsychotics in rats. *Nature Communications* **11**, 246 (2020).
11. Keshavan, M.S., Anderson, S. & Pettergrew, J.W. Is Schizophrenia due to excessive synaptic pruning in the prefrontal cortex? The Feinberg hypothesis revisited. *Journal of Psychiatric Research* **28**, 239-265 (1994).
12. Feinberg, I. Schizophrenia: caused by a fault in programmed synaptic elimination during adolescence? *Journal of psychiatric research* **17**, 319-334 (1982).
13. Yilmaz, M., *et al.* Overexpression of schizophrenia susceptibility factor human complement C4A promotes excessive synaptic loss and behavioral changes in mice. *Nature Neuroscience* **24**, 214-224 (2021).
14. Plitman, E., *et al.* Glutamate-mediated excitotoxicity in schizophrenia: a review. *European Neuropsychopharmacology* **24**, 1591-1605 (2014).
15. Kruse, A.O. & Bustillo, J.R. Glutamatergic dysfunction in Schizophrenia. *Translational Psychiatry* **12**, 500 (2022).
16. Bradshaw, N.J. & Korth, C. Protein misassembly and aggregation as potential convergence points for non-genetic causes of chronic mental illness. *Molecular psychiatry* **24**, 936-951 (2019).
17. Aryal, S., *et al.* Deep proteomics identifies shared molecular pathway alterations in synapses of patients with schizophrenia and bipolar disorder and mouse model. *Cell Reports* **42** (2023).
18. Seeley, W.W., Crawford, R.K., Zhou, J., Miller, B.L. & Greicius, M.D. Neurodegenerative diseases target large-scale human brain networks. *Neuron* **62**, 42-52 (2009).
19. Pak, V., *et al.* Distinctive whole-brain cell types predict tissue damage patterns in thirteen neurodegenerative conditions. *Elife* **12**, RP89368 (2024).
20. Wiesman, A.I., *et al.* Neurochemical organization of cortical proteinopathy and neurophysiology along the Alzheimer's disease continuum. *Alzheimer's & Dementia* (2024).
21. Fornito, A., Zalesky, A. & Breakspear, M. The connectomics of brain disorders. (2015).
22. Chopra, S., *et al.* Network-Based Spreading of Gray Matter Changes Across Different Stages of Psychosis. *JAMA Psychiatry* (2023).
23. Vogel, J.W., *et al.* Connectome-based modelling of neurodegenerative diseases: towards precision medicine and mechanistic insight. *Nature Reviews Neuroscience* **24**, 620-639 (2023).

24. Shafiei, G., *et al.* Spatial patterning of tissue volume loss in schizophrenia reflects brain network architecture. *Biological psychiatry* **87**, 727-735 (2020).
25. Bazinet, V., *et al.* Assortative mixing in micro-architecturally annotated brain connectomes. *Nature Communications* **14**, 2850 (2023).
26. Hansen, J.Y., *et al.* Local molecular and global connectomic contributions to cross-disorder cortical abnormalities. *Nature communications* **13**, 1-17 (2022).
27. Shafiei, G., *et al.* Global network structure and local transcriptomic vulnerability shape atrophy in sporadic and genetic behavioral variant frontotemporal dementia. *bioRxiv* (2021).
28. Zheng, Y.-Q., *et al.* Local vulnerability and global connectivity jointly shape neurodegenerative disease propagation. *PLoS biology* **17**, e3000495 (2019).
29. Brennand, K.J., *et al.* Modelling schizophrenia using human induced pluripotent stem cells. *Nature* **473**, 221-225 (2011).
30. Ishii, T., *et al.* In vitro modeling of the bipolar disorder and schizophrenia using patient-derived induced pluripotent stem cells with copy number variations of PCDH15 and RELN. *Eneuro* **6** (2019).
31. Wen, Z., *et al.* Synaptic dysregulation in a human iPS cell model of mental disorders. *Nature* **515**, 414-418 (2014).
32. Naujock, M., *et al.* Neuronal differentiation of induced pluripotent stem cells from schizophrenia patients in two-dimensional and in three-dimensional cultures reveals increased expression of the Kv4. 2 subunit DPP6 that contributes to decreased neuronal activity. *Stem cells and development* **29**, 1577-1587 (2020).
33. Rossano, S., *et al.* Assessment of a white matter reference region for 11C-UCB-J PET quantification. *Journal of Cerebral Blood Flow & Metabolism* **40**, 1890-1901 (2020).
34. Mertens, N., *et al.* Validation of Parametric methods for [11 C] UCB-J PET imaging using Subcortical White Matter as Reference tissue. *Molecular imaging and biology* **22**, 444-452 (2020).
35. Koole, M., *et al.* Quantifying SV2A density and drug occupancy in the human brain using [11 C] UCB-J PET imaging and subcortical white matter as reference tissue. *European journal of nuclear medicine and molecular imaging* **46**, 396-406 (2019).
36. van Erp, T.G.M., *et al.* Cortical Brain Abnormalities in 4474 Individuals With Schizophrenia and 5098 Control Subjects via the Enhancing Neuro Imaging Genetics Through Meta Analysis (ENIGMA) Consortium. *Biological Psychiatry* **84**, 644-654 (2018).
37. van Erp, T.G.M., *et al.* Subcortical brain volume abnormalities in 2028 individuals with schizophrenia and 2540 healthy controls via the ENIGMA consortium. *Molecular Psychiatry* **21**, 547-553 (2016).
38. Olabi, B., *et al.* Are there progressive brain changes in schizophrenia? A meta-analysis of structural magnetic resonance imaging studies. *Biological Psychiatry* **70**, 88-96 (2011).
39. Fusar-Poli, P., *et al.* Progressive brain changes in schizophrenia related to antipsychotic treatment? A meta-analysis of longitudinal MRI studies. *Neuroscience and Biobehavioral Reviews* **37**, 1680-1691 (2013).
40. Vita, A., De Peri, L., Deste, G. & Sacchetti, E. Progressive loss of cortical gray matter in schizophrenia: a meta-analysis and meta-regression of longitudinal MRI studies. *Translational Psychiatry* **2**, e190-e190 (2012).
41. Chopra, S., *et al.* Differentiating the effect of antipsychotic medication and illness on brain volume reductions in first-episode psychosis: A Longitudinal, Randomised, Triple-blind, Placebo-controlled MRI Study. *Neuropsychopharmacology* **46**, 1494-1501 (2021).
42. Haijma, S.V., *et al.* Brain Volumes in Schizophrenia: A Meta-Analysis in Over 18 000 Subjects. *Schizophrenia Bulletin* **39**, 1129-1138 (2013).
43. Weinberger, D.R., DeLisi, L.E., Perman, G.P., Targum, S. & Jed Wyatt, R. Computed Tomography in Schizophreniform Disorder and Other Acute Psychiatric Disorders. *Archives of General Psychiatry* **39**, 778-783 (1982).
44. Howes, O.D., Cummings, C., Chapman, G.E. & Shatalina, E. Neuroimaging in schizophrenia: an overview of findings and their implications for synaptic changes. *Neuropsychopharmacology*, 1-17 (2022).

45. Fornito, A., Yücel, M., Dean, B., Wood, S.J. & Pantelis, C. Anatomical abnormalities of the anterior cingulate cortex in schizophrenia: bridging the gap between neuroimaging and neuropathology. *Schizophrenia bulletin* **35**, 973-993 (2009).
46. Glausier, J.R. & Lewis, D.A. Dendritic spine pathology in schizophrenia. *Neuroscience* **251**, 90-107 (2013).
47. Lewandowski, K.E., Bouix, S., Ongur, D. & Shenton, M.E. Neuroprogression across the early course of psychosis. *Journal of psychiatry and brain science* **5** (2020).
48. Bustillo, J.R., *et al.* Glutamatergic and neuronal dysfunction in gray and white matter: a spectroscopic imaging study in a large schizophrenia sample. *Schizophrenia bulletin* **43**, 611-619 (2017).
49. Çetin, M.S., *et al.* Thalamus and posterior temporal lobe show greater inter-network connectivity at rest and across sensory paradigms in schizophrenia. *Neuroimage* **97**, 117-126 (2014).
50. Schaefer, A., *et al.* Local-Global Parcellation of the Human Cerebral Cortex from Intrinsic Functional Connectivity MRI. *Cerebral Cortex (New York, N.Y.: 1991)* **28**, 3095-3114 (2018).
51. Tian, Y., Margulies, D.S., Breakspear, M. & Zalesky, A. Topographic organization of the human subcortex unveiled with functional connectivity gradients. *Nature Neuroscience* **23**, 1421-1432 (2020).
52. Markello, R.D. & Misic, B. Comparing spatial null models for brain maps. *NeuroImage* **236**, 118052 (2021).
53. Alexander-Bloch, A.F., *et al.* On testing for spatial correspondence between maps of human brain structure and function. *Neuroimage* **178**, 540-551 (2018).
54. Segal, A., *et al.* Regional, circuit, and network heterogeneity of brain abnormalities in psychiatric disorders. *medRxiv*, 2022.2003.2007.22271986 (2022).
55. Yeo, B.T., *et al.* The organization of the human cerebral cortex estimated by intrinsic functional connectivity. *Journal of neurophysiology* (2011).
56. Vértes, P.E., *et al.* Gene transcription profiles associated with inter-modular hubs and connection distance in human functional magnetic resonance imaging networks. *Philosophical Transactions of the Royal Society B: Biological Sciences* **371**, 20150362 (2016).
57. von Economo, C.F. & Koskinas, G.N. *Die cytoarchitektonik der hirnrinde des erwachsenen menschen* (J. Springer, 1925).
58. Markello, R.D., *et al.* Neuromaps: structural and functional interpretation of brain maps. *Nature Methods* **19**, 1472-1479 (2022).
59. Jorstad, N.L., *et al.* Transcriptomic cytoarchitecture reveals principles of human neocortex organization. *Science* **382**, eadf6812 (2023).
60. Zhang, X.-H., *et al.* The Cellular Underpinnings of the Human Cortical Connectome. *bioRxiv* (2023).
61. Hawrylycz, M.J., *et al.* An anatomically comprehensive atlas of the adult human brain transcriptome. *Nature* **489**, 391-399 (2012).
62. Winkler, A.M., Renaud, O., Smith, S.M. & Nichols, T.E. Permutation inference for canonical correlation analysis. *NeuroImage* **220**, 117065 (2020).
63. Di Biase, M.A., *et al.* Linking Cortical and Connectional Pathology in Schizophrenia. *Schizophr Bull* **45**, 911-923 (2019).
64. Wannan, C.M.J., *et al.* Evidence for Network-Based Cortical Thickness Reductions in Schizophrenia. *American Journal of Psychiatry*, appi.ajp.2019.18040380 (2019).
65. Cauda, F., *et al.* The morphometric co-atrophy networking of schizophrenia, autistic and obsessive spectrum disorders. *Hum Brain Mapp* **39**, 1898-1928 (2018).
66. Jiang, Y., *et al.* Antipsychotics effects on network-level reconfiguration of cortical morphometry in first-episode schizophrenia. *medRxiv*, 2021.2001.2017.21249965 (2021).
67. Georgiadis, F., *et al.* Connectome architecture shapes large-scale cortical alterations in schizophrenia: a worldwide ENIGMA study. *Molecular Psychiatry*, 1-13 (2024).
68. Cauda, F., *et al.* Brain structural alterations are distributed following functional, anatomic and genetic connectivity. *Brain* **141**, 3211-3232 (2018).

69. Raj, A., Kuceyeski, A. & Weiner, M. A network diffusion model of disease progression in dementia. *Neuron* **73**, 1204-1215 (2012).
70. Cai, H., *et al.* Radiosynthesis of 11C-levetiracetam: a potential marker for PET imaging of SV2A expression. *ACS medicinal chemistry letters* **5**, 1152-1155 (2014).
71. Custer, K.L., Austin, N.S., Sullivan, J.M. & Bajjalieh, S.M. Synaptic vesicle protein 2 enhances release probability at quiescent synapses. *Journal of Neuroscience* **26**, 1303-1313 (2006).
72. Buckley, K. & Kelly, R.B. Identification of a transmembrane glycoprotein specific for secretory vesicles of neural and endocrine cells. *The Journal of cell biology* **100**, 1284-1294 (1985).
73. Bajjalieh, S.M., Frantz, G., Weimann, J.M., McConnell, S.K. & Scheller, R. Differential expression of synaptic vesicle protein 2 (SV2) isoforms. *Journal of Neuroscience* **14**, 5223-5235 (1994).
74. Nabulsi, N.B., *et al.* Synthesis and preclinical evaluation of 11C-UCB-J as a PET tracer for imaging the synaptic vesicle glycoprotein 2A in the brain. *Journal of Nuclear Medicine* **57**, 777-784 (2016).
75. Finnema, S.J., *et al.* Kinetic evaluation and test–retest reproducibility of [11C] UCB-J, a novel radioligand for positron emission tomography imaging of synaptic vesicle glycoprotein 2A in humans. *Journal of Cerebral Blood Flow & Metabolism* **38**, 2041-2052 (2018).
76. Bastin, C., *et al.* In vivo imaging of synaptic loss in Alzheimer's disease with [18F] UCB-H positron emission tomography. *European Journal of Nuclear Medicine and Molecular Imaging* **47**, 390-402 (2020).
77. Whiteside, D.J., *et al.* Synaptic density affects clinical severity via network dysfunction in syndromes associated with frontotemporal lobar degeneration. *Nature Communications* **14**, 8458 (2023).
78. Saadabad, F.E., *et al.* Measuring Synaptic Density and Dopamine Transporter Availability in Parkinson's Disease: A PET Imaging Study with 11C-UCB-J and 18F-FE-PE2I (P7-3.007). in *Neurology* 3770 (AAN Enterprises, 2024).
79. Chang, Y.Y., *et al.* A study to determine the mechanisms underlying changes in synaptic vesicle glycoprotein 2A density in Alzheimer's disease. *Alzheimer's & Dementia* **19**, e082561 (2023).
80. Ripke, S., *et al.* Biological insights from 108 schizophrenia-associated genetic loci. *Nature* **511**, 421-427 (2014).
81. Zhou, L., *et al.* Tau association with synaptic vesicles causes presynaptic dysfunction. *Nature Communications* **8**, 15295 (2017).
82. Parodi, J., *et al.* β-amyloid causes depletion of synaptic vesicles leading to neurotransmission failure. *Journal of Biological Chemistry* **285**, 2506-2514 (2010).
83. Cabin, D.E., *et al.* Synaptic vesicle depletion correlates with attenuated synaptic responses to prolonged repetitive stimulation in mice lacking α-synuclein. *Journal of Neuroscience* **22**, 8797-8807 (2002).
84. Soustek, Z. Ultrastructure of cortical synapses in the brain of schizophrenics. *Zentralblatt fur Allgemeine Pathologie u. Pathologische Anatomie* **135**, 25-32 (1989).
85. Ong, W. & Garey, L. Ultrastructural features of biopsied temporopolar cortex (area 38) in a case of schizophrenia. *Schizophrenia research* **10**, 15-27 (1993).
86. Rees, S. A quantitative electron microscopic study of the ageing human cerebral cortex. *Acta Neuropathologica* **36**, 347-362 (1976).
87. Krassner, M.M., *et al.* Postmortem changes in brain cell structure: a review. *Free Neuropathology* **4** (2023).
88. Collins, M.A., *et al.* Accelerated cortical thinning precedes and predicts conversion to psychosis: The NAPLS3 longitudinal study of youth at clinical high-risk. *Mol Psychiatry* (2022).
89. Weinberger, D.R. & Radulescu, E. Structural Magnetic Resonance Imaging All Over Again. *JAMA Psychiatry* (2020).
90. Zipursky, R.B., Reilly, T.J. & Murray, R.M. The myth of schizophrenia as a progressive brain disease. *Schizophr Bull* **39**, 1363-1372 (2013).
91. Weinberger, D.R. & Radulescu, E. Finding the Elusive Psychiatric "Lesion" With 21st-Century Neuroanatomy: A Note of Caution. *American Journal of Psychiatry* **173**, 27-33 (2016).

92. Toyonaga, T., *et al.* The regional pattern of age-related synaptic loss in the human brain differs from gray matter volume loss: in vivo PET measurement with [11C] UCB-J. *European Journal of Nuclear Medicine and Molecular Imaging* **51**, 1012-1022 (2024).
93. Hirsch, E., Graybiel, A.M. & Agid, Y.A. Melanized dopaminergic neurons are differentially susceptible to degeneration in Parkinson's disease. *Nature* **334**, 345-348 (1988).
94. Lotharius, J. & Brundin, P. Pathogenesis of parkinson's disease: dopamine, vesicles and α-synuclein. *Nature Reviews Neuroscience* **3**, 932-942 (2002).
95. Filippi, M., *et al.* Multiple sclerosis. *Nature Reviews Disease Primers* **4**, 43 (2018).
96. Mahad, D.H., Trapp, B.D. & Lassmann, H. Pathological mechanisms in progressive multiple sclerosis. *The Lancet Neurology* **14**, 183-193 (2015).
97. Grothe, M.J., Teipel, S.J. & Initiative, A.s.D.N. Spatial patterns of atrophy, hypometabolism, and amyloid deposition in Alzheimer's disease correspond to dissociable functional brain networks. *Human brain mapping* **37**, 35-53 (2016).
98. Baker, J.T., *et al.* Disruption of Cortical Association Networks in Schizophrenia and Psychotic Bipolar Disorder. *JAMA psychiatry* **71**, 109-118 (2014).
99. Busatto, G.F., *et al.* Correlation between reduced in vivo benzodiazepine receptor binding and severity of psychotic symptoms in schizophrenia. *American Journal of Psychiatry* **154**, 56-63 (1997).
100. Selvaraj, S., Arnone, D., Cappai, A. & Howes, O. Alterations in the serotonin system in schizophrenia: a systematic review and meta-analysis of postmortem and molecular imaging studies. *Neuroscience & Biobehavioral Reviews* **45**, 233-245 (2014).
101. Frankle, W.G., *et al.* In vivo measurement of GABA transmission in healthy subjects and schizophrenia patients. *American Journal of Psychiatry* **172**, 1148-1159 (2015).
102. Borgan, F., *et al.* In vivo availability of cannabinoid 1 receptor levels in patients with first-episode psychosis. *JAMA psychiatry* **76**, 1074-1084 (2019).
103. Consortium, T.S.W.G.o.t.P.G., Ripke, S., Walters, J.T. & O'Donovan, M.C. Mapping genomic loci prioritises genes and implicates synaptic biology in schizophrenia. *medRxiv*, 2020.2009.2012.20192922 (2020).
104. Owen, M.J., Legge, S.E., Rees, E., Walters, J.T.R. & O'Donovan, M.C. Genomic findings in schizophrenia and their implications. *Molecular Psychiatry* **28**, 3638-3647 (2023).
105. Batiuk, M.Y., *et al.* Upper cortical layer–driven network impairment in schizophrenia. *Science Advances* **8**, eabn8367 (2022).
106. Ruzicka, W.B., *et al.* Single-cell multi-cohort dissection of the schizophrenia transcriptome. *Science* **384**, eadg5136 (2024).
107. Hoftman, G.D., Datta, D. & Lewis, D.A. Layer 3 Excitatory and Inhibitory Circuitry in the Prefrontal Cortex: Developmental Trajectories and Alterations in Schizophrenia. *Biological Psychiatry* **81**, 862-873 (2017).
108. Shafiei, G., *et al.* Network structure and transcriptomic vulnerability shape atrophy in frontotemporal dementia. *Brain* (2022).
109. Pantelis, C., *et al.* Neuroanatomical abnormalities before and after onset of psychosis: a cross-sectional and longitudinal MRI comparison. *The Lancet* **361**, 281-288 (2003).
110. Fusar-Poli, P., *et al.* Neuroanatomy of vulnerability to psychosis: A voxel-based meta-analysis. *Neuroscience & Biobehavioral Reviews* **35**, 1175-1185 (2011).
111. Borgwardt, S.J., *et al.* Structural brain abnormalities in individuals with an at-risk mental state who later develop psychosis. *The British Journal of Psychiatry* **191**, s69-s75 (2007).
112. Jiang, Y., *et al.* Neurostructural subgroup in 4291 individuals with schizophrenia identified using the subtype and stage inference algorithm. *Nature communications* **15**, 5996 (2024).
113. Jiang, Y., *et al.* Neuroimaging biomarkers define neurophysiological subtypes with distinct trajectories in schizophrenia. *Nature Mental Health* **1**, 186-199 (2023).
114. Pils, M., *et al.* Disrupted in schizophrenia 1 protein aggregates in cerebrospinal fluid are elevated in patients with first episode psychosis. *Psychiatry and clinical neurosciences* **77**, 665-671 (2023).

115. Samardžija, B., Renner, É., Palkovits, M. & Bradshaw, N.J. Protein aggregation of DISC1, as assayed by insolubility, varies across the brain of an individual with schizophrenia and Alzheimer's disease. *medRxiv*, 2023.2008. 2001.23293413 (2023).
116. Nucifora, L.G., *et al.* Increased Protein Insolubility in Brains From a Subset of Patients With Schizophrenia. *Am J Psychiatry* **176**, 730-743 (2019).
117. Trossbach, S., *et al.* Misassembly of full-length Disrupted-in-Schizophrenia 1 protein is linked to altered dopamine homeostasis and behavioral deficits. *Molecular psychiatry* **21**, 1561-1572 (2016).
118. Dahoun, T., Trossbach, S., Brandon, N., Korth, C. & Howes, O. The impact of Disrupted-in-Schizophrenia 1 (DISC1) on the dopaminergic system: a systematic review. *Translational psychiatry* **7**, e1015-e1015 (2017).
119. Zhu, S., Abounit, S., Korth, C. & Zurzolo, C. Transfer of disrupted-in-schizophrenia 1 aggregates between neuronal-like cells occurs in tunnelling nanotubes and is promoted by dopamine. *Open Biology* **7**, 160328 (2017).
120. Guo, J.L. & Lee, V.M. Cell-to-cell transmission of pathogenic proteins in neurodegenerative diseases. *Nature medicine* **20**, 130-138 (2014).
121. Haroon, E., Miller, A.H. & Sanacora, G. Inflammation, Glutamate, and Glia: A Trio of Trouble in Mood Disorders. *Neuropsychopharmacology* **42**, 193-215 (2017).
122. Patel, P.K., Leathem, L.D., Currin, D.L. & Karlsgodt, K.H. Adolescent neurodevelopment and vulnerability to psychosis. *Biological Psychiatry* **89**, 184-193 (2021).
123. Howes, O. & McCutcheon, R. Inflammation and the neural diathesis-stress hypothesis of schizophrenia: a reconceptualization. *Translational psychiatry* **7**, e1024-e1024 (2017).
124. Wolfers, T., *et al.* Mapping the Heterogeneous Phenotype of Schizophrenia and Bipolar Disorder Using Normative Models. *JAMA Psychiatry* (2018).
125. Segal, A., *et al.* Regional, circuit and network heterogeneity of brain abnormalities in psychiatric disorders. *Nature Neuroscience* **26**, 1613-1629 (2023).
126. Maier-Hein, K.H., *et al.* The challenge of mapping the human connectome based on diffusion tractography. *Nature Communications* **8**, 1349 (2017).
127. Schiavi, S., *et al.* A new method for accurate in vivo mapping of human brain connections using microstructural and anatomical information. *Science advances* **6**, eaba8245-eaba8245 (2020).
128. Carson, R.E., Barker, W.C., Liow, J.-S. & Johnson, C.A. Design of a motion-compensation OSEM list-mode algorithm for resolution-recovery reconstruction for the HRRT. in *2003 IEEE Nuclear Science Symposium. Conference Record (IEEE Cat. No. 03CH37515)* 3281-3285 (IEEE, 2003).
129. Jin, X., *et al.* List-mode reconstruction for the Biograph mCT with physics modeling and event-by-event motion correction. *Physics in Medicine & Biology* **58**, 5567 (2013).
130. Müller-Gärtner, H.W., *et al.* Measurement of radiotracer concentration in brain gray matter using positron emission tomography: MRI-based correction for partial volume effects. *Journal of Cerebral Blood Flow & Metabolism* **12**, 571-583 (1992).
131. Naganawa, M., *et al.* Noninvasive quantification of 18F-SynVesT-1 binding using simplified reference tissue model 2. (Soc Nuclear Med, 2022).
132. Wu, Y. & Carson, R.E. Noise reduction in the simplified reference tissue model for neuroreceptor functional imaging. *Journal of Cerebral Blood Flow & Metabolism* **22**, 1440-1452 (2002).
133. Ashburner, J., *et al.* SPM12 manual. *Wellcome Trust Centre for Neuroimaging, London, UK* **2464** (2014).
134. Lorio, S., *et al.* New tissue priors for improved automated classification of subcortical brain structures on MRI. *Neuroimage* **130**, 157-166 (2016).
135. Gaser, C., *et al.* CAT–A computational anatomy toolbox for the analysis of structural MRI data. *biorxiv*, 2022.2006. 2011.495736 (2022).
136. Scholtens, L.H., de Reus, M.A., de Lange, S.C., Schmidt, R. & van den Heuvel, M.P. An MRI Von Economo – Koskinas atlas. *NeuroImage* **170**, 249-256 (2018).
137. Hansen, J.Y., *et al.* Mapping neurotransmitter systems to the structural and functional organization of the human neocortex. *bioRxiv*, 2021.2010.2028.466336 (2022).

138. Jorstad, N.L., *et al.* Comparative transcriptomics reveals human-specific cortical features. *Science* **382**, eade9516 (2023).
139. Zimmermann, J., Griffiths, J.D. & McIntosh, A.R. Unique Mapping of Structural and Functional Connectivity on Cognition. *Journal of Neuroscience* **38**, 9658-9667 (2018).
140. Van Essen, D.C., *et al.* The WU-Minn human connectome project: an overview. *Neuroimage* **80**, 62-79 (2013).
141. Jenkinson, M., Bannister, P., Brady, M. & Smith, S. Improved optimization for the robust and accurate linear registration and motion correction of brain images. *Neuroimage* **17**, 825-841 (2002).
142. Glasser, M.F., *et al.* The minimal preprocessing pipelines for the Human Connectome Project. *Neuroimage* **80**, 105-124 (2013).
143. Fischl, B., *et al.* Whole brain segmentation: automated labeling of neuroanatomical structures in the human brain. *Neuron* **33**, 341-355 (2002).
144. Arnatkeviciute, A., *et al.* Genetic influences on hub connectivity of the human connectome. *Nature Communications* **12**, 4237 (2021).
145. Jeurissen, B., Tournier, J.-D., Dhollander, T., Connelly, A. & Sijbers, J. Multi-tissue constrained spherical deconvolution for improved analysis of multi-shell diffusion MRI data. *NeuroImage* **103**, 411-426 (2014).
146. Tournier, J.D., *et al.* MRtrix3: A fast, flexible and open software framework for medical image processing and visualisation. *NeuroImage* **202**, 116137 (2019).
147. Tournier, J.D., Calamante, F. & Connelly, A. Robust determination of the fibre orientation distribution in diffusion MRI: Non-negativity constrained super-resolved spherical deconvolution. *NeuroImage* **35**, 1459-1472 (2007).
148. Smith, R.E., Tournier, J.D., Calamante, F. & Connelly, A. Anatomically-constrained tractography: improved diffusion MRI streamlines tractography through effective use of anatomical information. *Neuroimage* **62**, 1924-1938 (2012).
149. Smith, R.E., Tournier, J.-D., Calamante, F. & Connelly, A. SIFT2: Enabling dense quantitative assessment of brain white matter connectivity using streamlines tractography. *Neuroimage* **119**, 338-351 (2015).
150. Fischl, B. FreeSurfer. *Neuroimage* **62**, 774-781 (2012).
151. Jenkinson, M., Beckmann, C.F., Behrens, T.E., Woolrich, M.W. & Smith, S.M. FSL. *Neuroimage* **62**, 782-790 (2012).
152. Schilling, K.G., *et al.* Limits to anatomical accuracy of diffusion tractography using modern approaches. *Neuroimage* **185**, 1-11 (2019).
153. Betzel, R.F., Griffa, A., Hagmann, P. & Mišić, B. Distance-dependent consensus thresholds for generating group-representative structural brain networks. *Netw Neurosci* **3**, 475-496 (2019).
154. Andersson, J.L., Skare, S. & Ashburner, J. How to correct susceptibility distortions in spin-echo echo-planar images: application to diffusion tensor imaging. *Neuroimage* **20**, 870-888 (2003).
155. Salimi-Khorshidi, G., *et al.* Automatic denoising of functional MRI data: combining independent component analysis and hierarchical fusion of classifiers. *Neuroimage* **90**, 449-468 (2014).
156. Markello, R.D., *et al.* Standardizing workflows in imaging transcriptomics with the abagen toolbox. *elife* **10**, e72129 (2021).
157. Arnatkevic□iūtė, A., Fulcher, B.D. & Fornito, A. A practical guide to linking brain-wide gene expression and neuroimaging data. *Neuroimage* **189**, 353-367 (2019).
158. Quackenbush, J. Microarray data normalization and transformation. *Nature genetics* **32**, 496-501 (2002).
159. Fulcher, B.D., Little, M.A. & Jones, N.S. Highly comparative time-series analysis: the empirical structure of time series and their methods. *Journal of the Royal Society Interface* **10**, 20130048 (2013).
160. Raj, A., *et al.* Network diffusion model of progression predicts longitudinal patterns of atrophy and metabolism in Alzheimer's disease. *Cell reports* **10**, 359-369 (2015).

Supplement

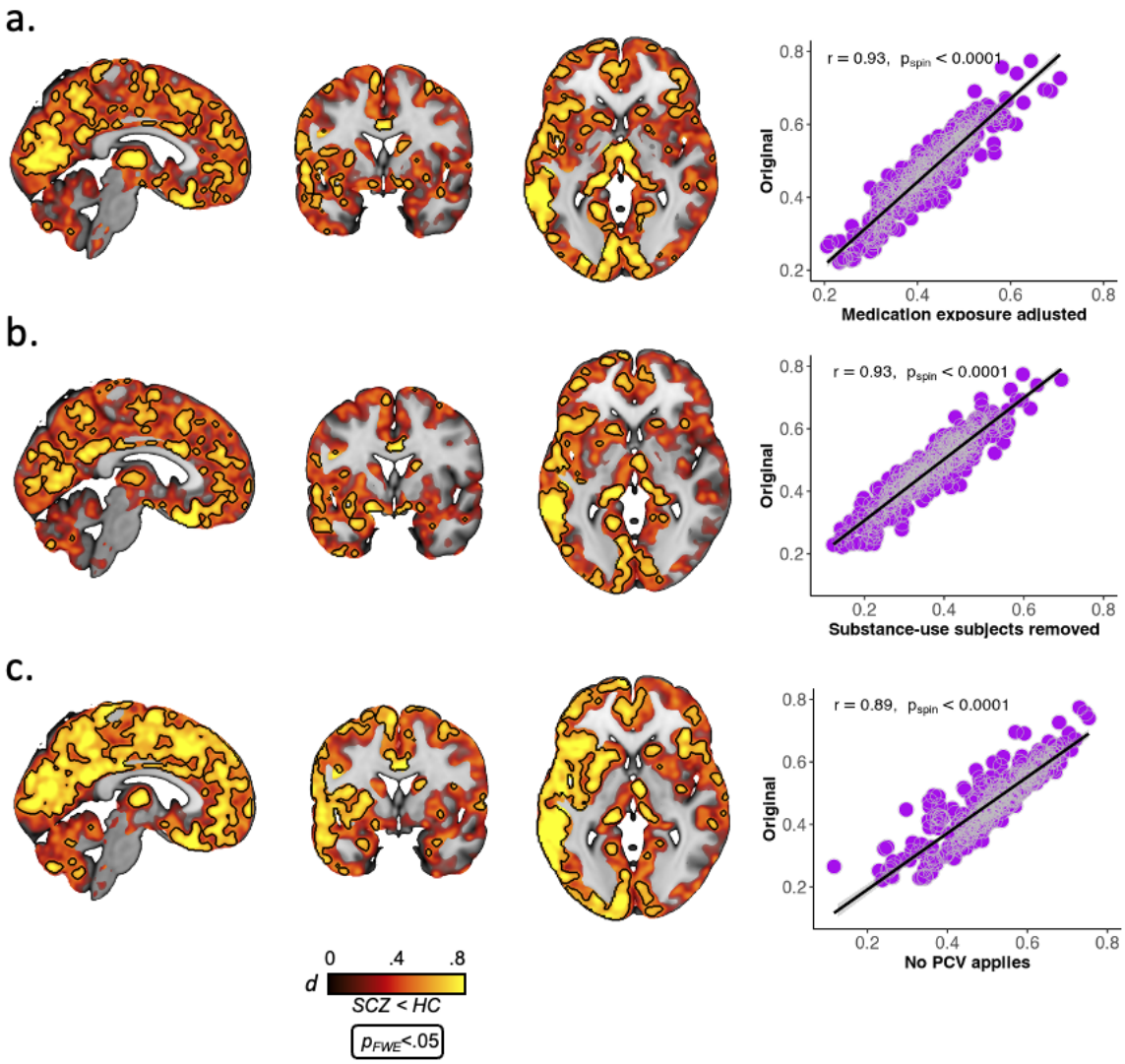

SFig. 1 – Effect size maps for group difference in synaptic density after adjusting for medication exposure **(a)**, removal of subjects with substance abuse **(b)**, removing partial volume correction (**c**; PVC). Black outline shows voxel-level FWE-corrected significant areas. Scatter plots show association between each parcellated effect size map and the group difference maps used in the primary analysis (Fig. 1A).

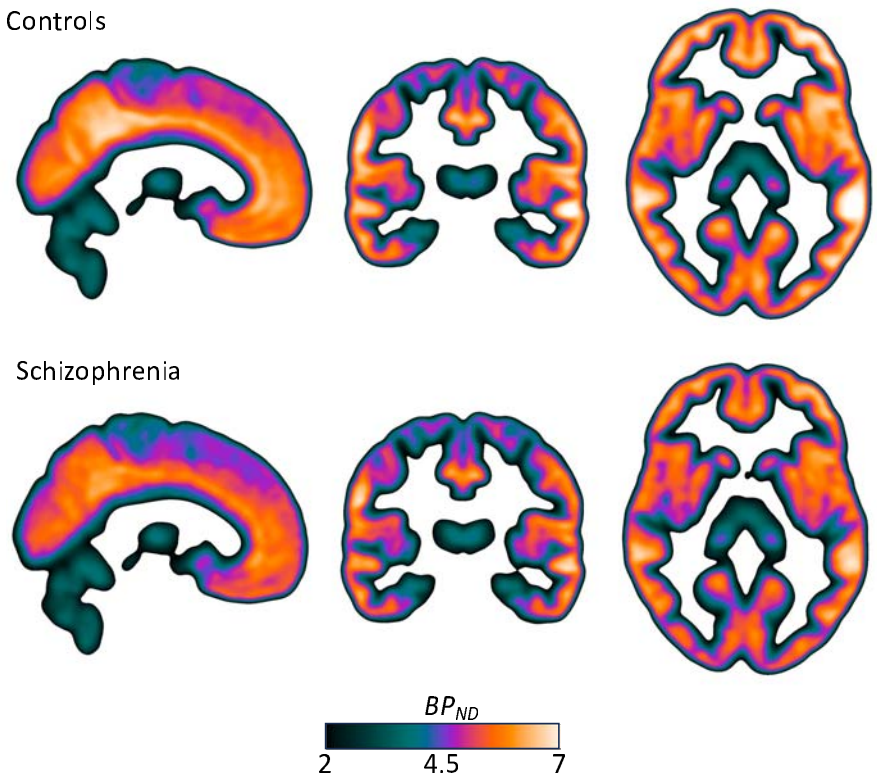

SFig. 2 – Mean of parametric BP_{ND} images for controls (top) and patients (bottom). Linear interpolation has been applied to the images for visualization.

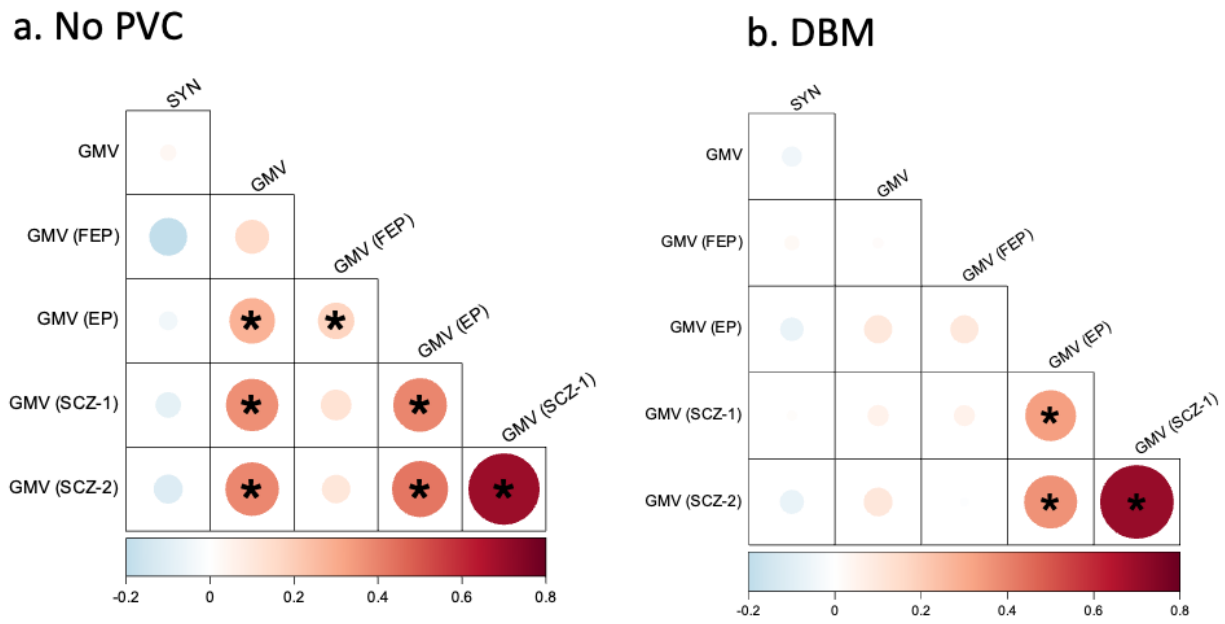

SFig. 2 – Spatial correlation (Pearsons r) between parcellated synaptic density alterations (SYN) and gray matter volume (GMV) within the current sample (top left box in each panel), as well as four independent samples including antipsychotic-naive first-episode psychosis (FEP), early psychosis (EP) and two established schizophrenia (SCZ) cohorts. All other boxes represent correlations between GMV maps between the current and independent samples. Asterisks (*) indicate statistical significance ( ) completed to spatial autocorrelation preserving null models. **(a)** Correlations when synaptic density data is not partial volume corrected (PVC) and **(b)** when DBM is used to measure grey matter alterations, instead of VBM.

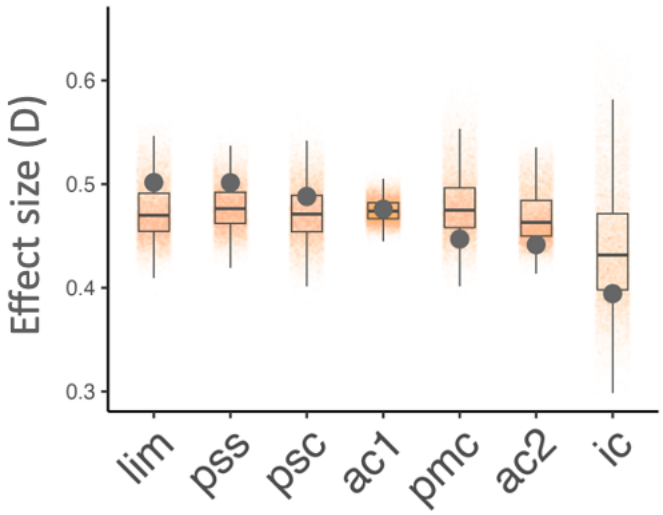

SFig. 4 – Boxplots showing preferential accumulation of synaptic deficits within each of the 7 cytoarchitectonic network of laminar differentiation. Grey dots represent observed mean effect-size of lower synaptic density in individuals with schizophrenia, with orange dots representing null mean effect sizes generated using spatial-autocorrelation preserving models. No significant findings were detected.

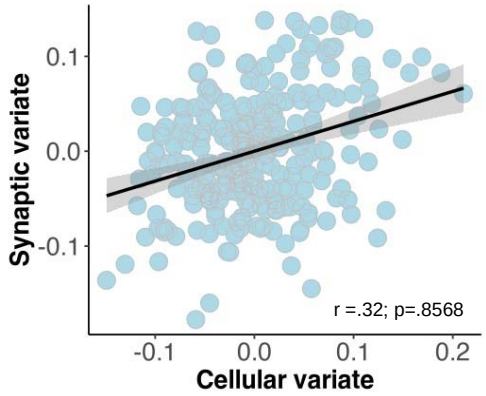

SFig. 5 – Canonical correlation between regional synaptic deficits and normative cell type density. The synaptic variate (y-axis) in this case is normalized regional synaptic deficit effect size, whereas the cellular variate is a normalized weighted combination 24 different cell densities. The non-parametric -value was computed using spatial-autocorrelation preserving models.

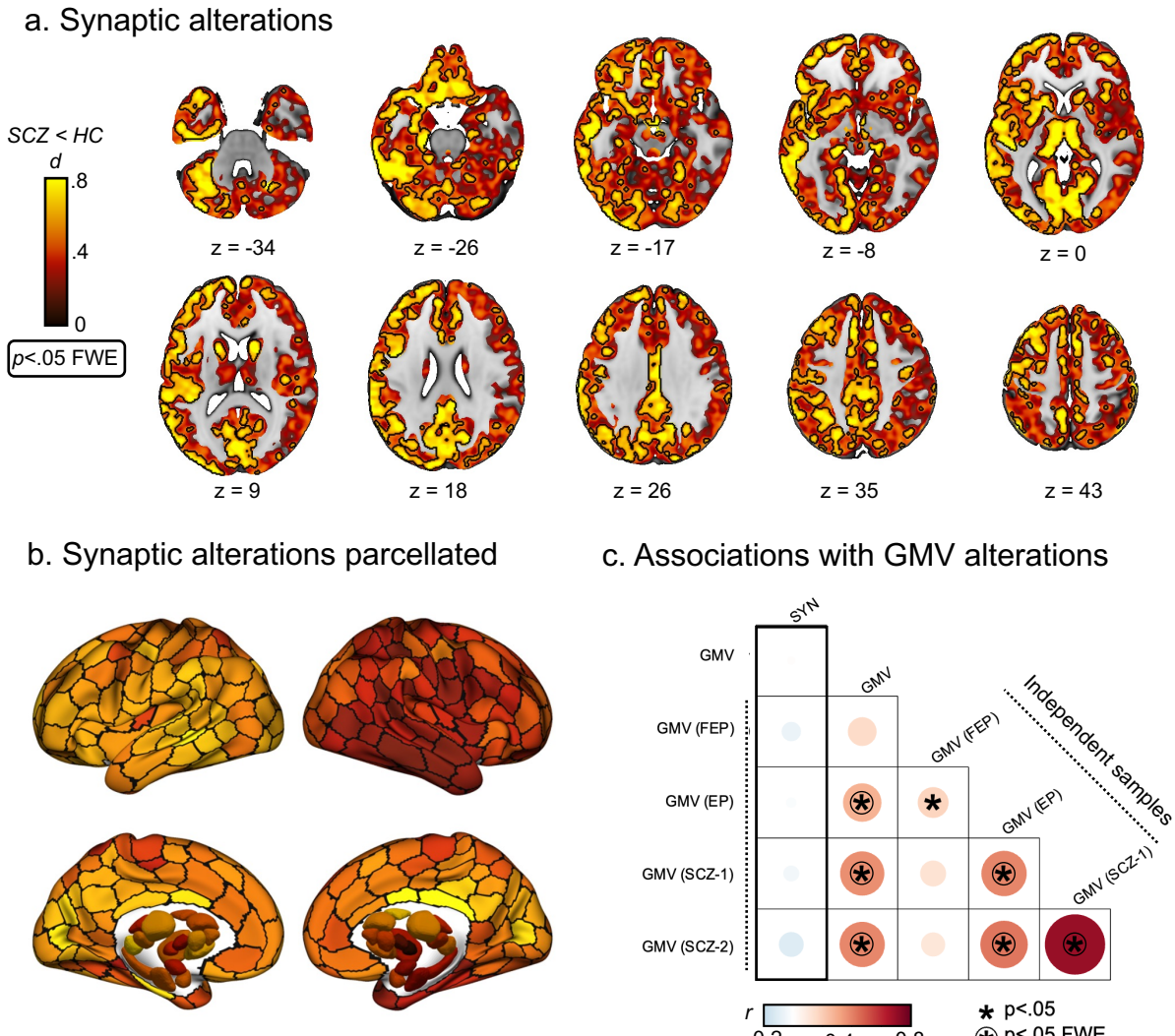
a. Synaptic alterations
SCZ < HC
d
.8
.4
0
p<.05 FWE
z = -34
z = -26
z = -17
z = -8
z = 0
z = 9
z = 18
z = 26
z = 35
z = 43
b. Synaptic alterations parcellated
c. Associations with GMV alterations
SYN
GMV
GMV (FEP)
GMV (EP)
GMV (SCZ-1)
GMV (SCZ-2)
Independent samples
r
-0.2
0.4
0.8
p<.05
p<.05 FWE

Functional network enrichment

a.

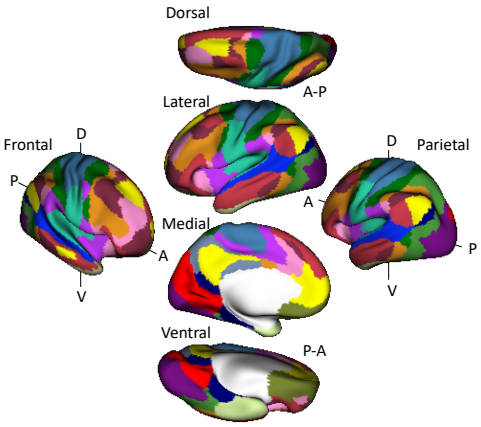

b.

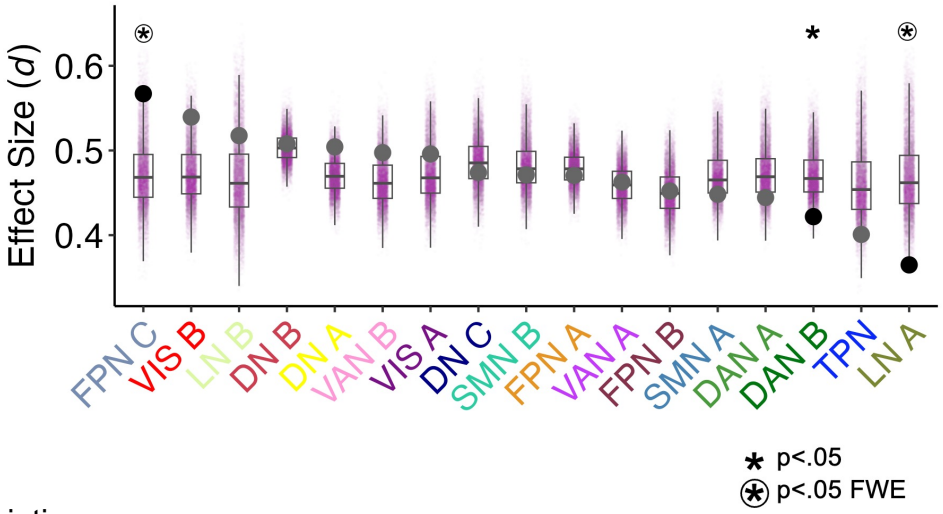

Receptors and transporter associations

c.

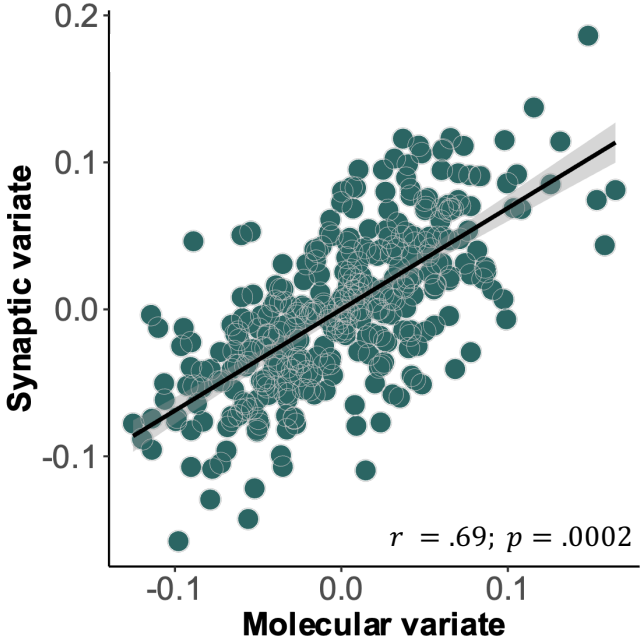

d.

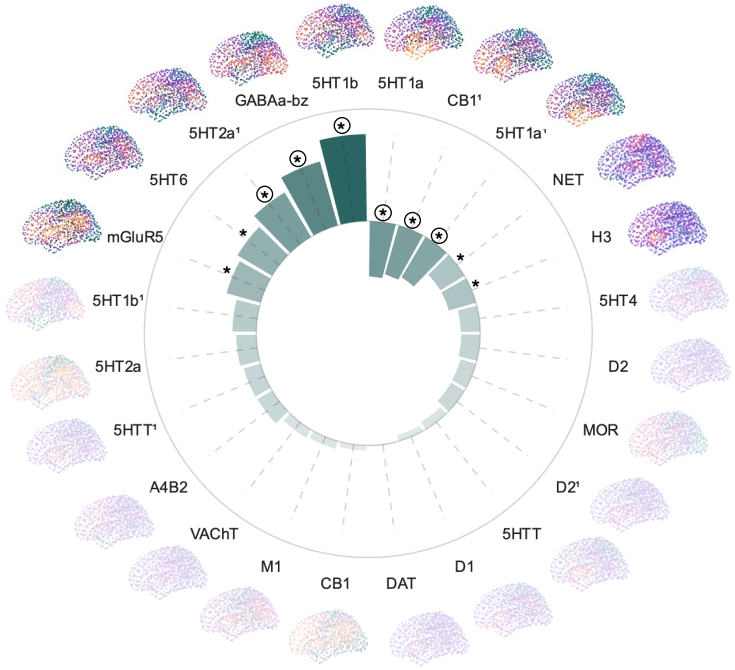

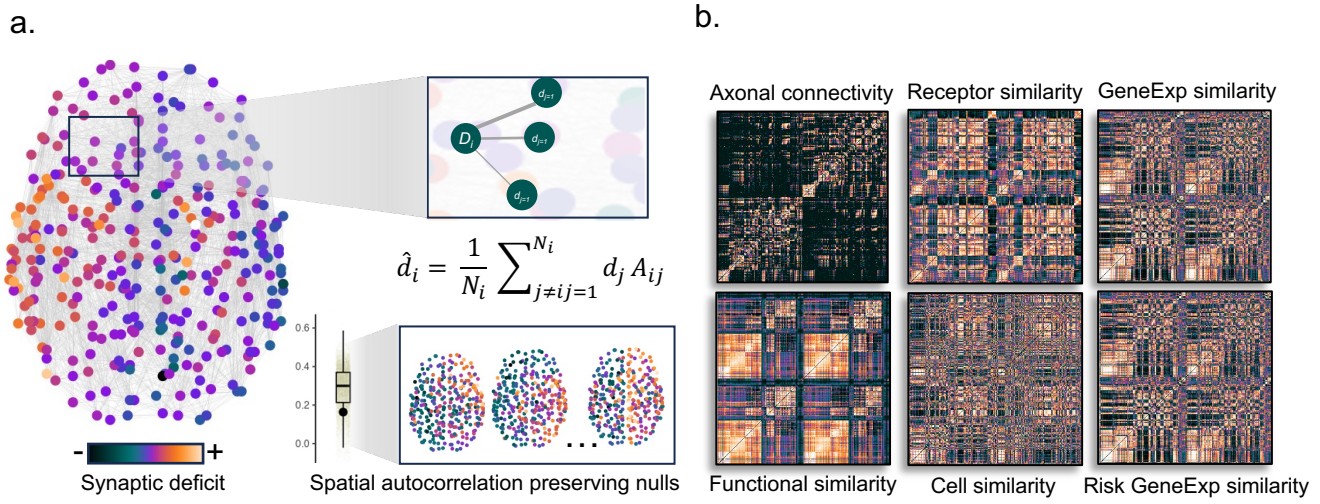
a.
b.
Synaptic deficit
Spatial autocorrelation preserving nulls
Axonal connectivity
Receptor similarity
GeneExp similarity
Functional similarity
Cell similarity
Risk GeneExp similarity

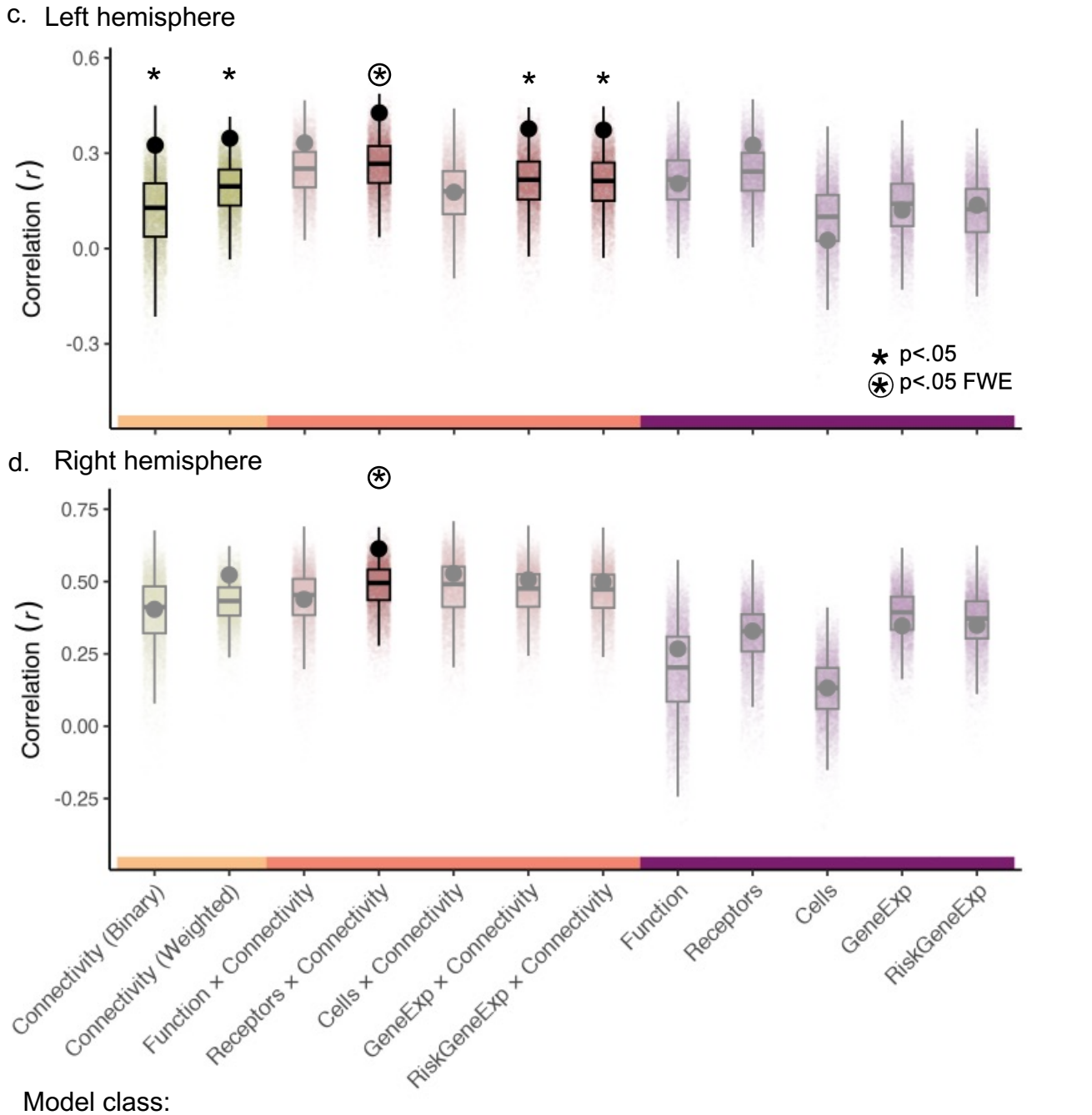
c. Left hemisphere
Correlation (r)
0.6
0.3
0.0
-0.3
* p<.05
⊛ p<.05 FWE
d. Right hemisphere
Correlation (r)
0.75
0.50
0.25
0.00
-0.25
Connectivity (Binary)
Connectivity (Weighted)
Function × Connectivity
Receptors × Connectivity
Cells × Connectivity
GeneExp × Connectivity
RiskGeneExp × Connectivity
Function
Receptors
Cells
GeneExp
RiskGeneExp
Model class:
Connectivity
Joint (Connectivity × Regional vulnerability)
Regional vulnerability

a. Network Diffusion Model

$$f(t) = e^{-\beta H t} f_0$$

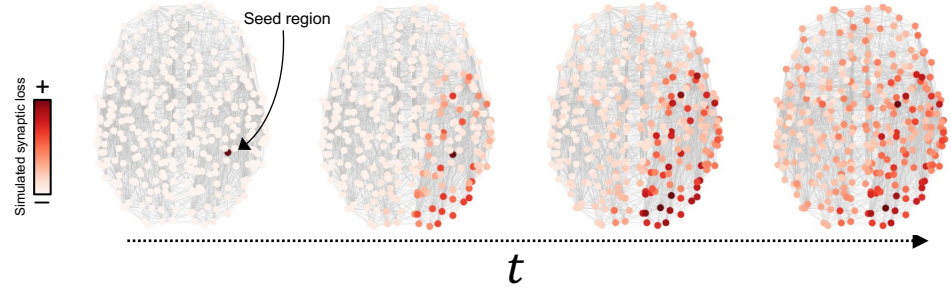

b. Regional performance

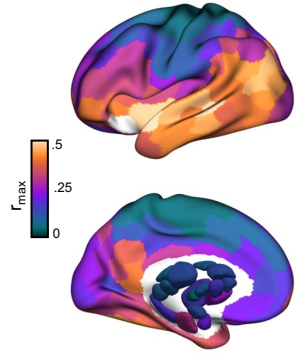

c. Significant regions

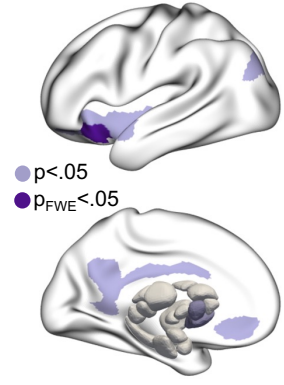
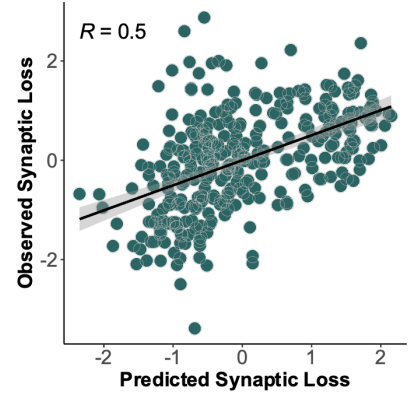
d. Significant region performance